The Planetary Science Journal, 5:214 (19pp), 2024 September https://doi.org/10.3847/PSJ/ad72eb

Impact Momentum Transfer—Insights from Numerical Simulation of Impacts on Large Boulders of Asteroids

Kaiyi Dai[1,2,5], Xi-Zi Luo[1,5], Meng-Hua Zhu[1], Gareth S. Collins[2], Thomas Davison[2], Robert Luther[3], and Kai Wünnemann[3,4]
[1] State Key Laboratory of Lunar and Planetary Sciences, Macau University of Science and Technology, Taipa, Macau; mhzhu@must.edu.mo
[2] Department of Earth Science and Engineering, Imperial College London, London, UK
[3] Museum für Naturkunde, Leibniz Institute for Evolution and Biodiversity Science, Berlin, Germany
[4] Institute of Geological Sciences, Planetary Sciences and Remote Sensing, Freie Universität Berlin, Berlin, Germany
Received 2024 June 18; revised 2024 August 19; accepted 2024 August 20; published 2024 September 30

Abstract

Asteroids pose potential hazards to Earth. The recent NASA Double Asteroid Redirection Test mission successfully demonstrated the change of an asteroid's orbit by a kinetic impactor. This study focuses on impact-induced vertical momentum transfer efficiency ($\beta-1$) considering various impact angles and subsurface boulder arrangements. Utilizing the iSALE-3D shock physics code, we simulate oblique impacts on different subsurface boulder configurations. Our results show that vertical ejecta momentum decreases with obliquity, with buried boulders inducing an anti-armoring effect. We define the direct impact-contacted boulder as the primary boulder and the surrounding boulders as secondary. The anti-armoring effect is most pronounced when the primary boulder is just below the surface, amplifying $\beta-1$ by 50%. Impact angles between 60° and 75° exhibit a critical drop in ejecta momentum. An in-depth exploration of subsurface boulder arrangements reveals that secondary boulders have a minimal effect on vertical momentum transfer efficiency. Varying the size and separation of secondary boulders suggests that these subsurface features can either enhance or diminish the overall $\beta-1$, providing insights into the dynamics of rubble-pile asteroids. In addition, impact melting is explored in our simulations, which suggests a minimal melt retention on Dimorphos's surface. Volumes of retained melt differ by an order of magnitude for impacts on the homogeneous regolith and on targets with buried boulders. In summary, this study provides insights into the effect of subsurface boulders and impact angles on vertical momentum transfer efficiency, which is crucial for understanding asteroid deflection by a kinetic impactor.

Unified Astronomy Thesaurus concepts: Impact phenomena (779); Planetary surfaces (2113)

1. Introduction

Asteroids are thought to consist of primordial materials that are crucial for early planet formation. They have shaped Earth's formation, atmosphere, and surface structure in the past. Today, they still pose a potential hazard (C. R. Chapman & D. Morrison 1994), which in the most extreme scenarios could cause a mass extinction that significantly changes the biological evolution of Earth. Therefore, how to reduce the threat of asteroid impact to humanity is critical for planetary defense. The successful NASA Double Asteroid Redirection Test (DART) mission on 2022 September 26 demonstrates the feasibility of using a kinetic impact to alter an asteroid's orbit (R. T. Daly et al. 2023). The target asteroid Dimorphos is the secondary member of the Didymos binary asteroid system (65803; A. F. Cheng et al. 2016). Dimorphos has a volume-equivalent diameter of 151 m (R. T. Daly et al. 2023). Its orbital period was reduced by 33.0 ± 1 minutes after being impacted by the DART spacecraft head-on (C. A. Thomas et al. 2023). The impact produces substantial ejecta, which was directly observed by the LICIACube flyby (E. Dotto & A. Zinzi 2023). The momentum transfer efficiency (β), defined by the total momentum change of Dimorphos divided by the spacecraft's incident momentum (mU), is estimated to range from 2.2 to 4.9, depending on the mass and density of Dimorphos (A. F. Cheng et al. 2023). The ESA Hera mission spacecraft will rendezvous with Dimorphos and investigate the physical properties of the asteroid, including the DART impact site, in early 2027 (P. Michel 2022). Until then, the properties of the crater and the β factor must be evaluated by numerical simulations.

Impact ejecta have a crucial effect on the deflection efficiency of a kinetic impact. During the impact, most ejecta will rapidly escape from the low gravitational attraction of the asteroid. This detachment process enhances the momentum transfer efficiency to the target and in a simple head-on collision can be quantified by the scalar momentum enhancement factor:

$$\beta-1=\frac{P_{\rm ej}}{mU}, \tag{1}$$

where $P_{\rm ej}$ is the total ejecta momentum in the anti-impact direction, m is the mass of the impacting spacecraft, and U is the impact speed. If $\beta-1=1$, it suggests that the ejecta momentum has the same contribution for deflection as the impactor. If $\beta-1>1$, it implies that the total ejecta momentum is bigger than the momentum carried by the impactor.

Dimorphos, the target of DART, is likely a rubble-pile asteroid and features a boulder-strewn surface as revealed by DART images (R. T. Daly et al. 2023). According to O. Barnouin et al. (2024), Dimorphos was formed through the gravitational accretion of debris from Didymos. Both asteroids are characterized by large surface boulders relative to their sizes, indicating that they are rubble piles. The size–frequency

[5] Equal contributions to this work.

distribution of large boulders (greater than 5 m on Dimorphos and greater than 22.8 m on Didymos) further supports the rubble-pile nature of both asteroids (M. Pajola et al. 2024). Additionally, the morphology of the boulders on Dimorphos is similar to those found on other rubble-pile asteroids, such as Itokawa, Ryugu, and Bennu (C. Q. Robin et al. 2024).

The surface and internal structures of rubble-pile asteroids revealed by previous missions vary (e.g., S. Abe et al. 2006; B. Rozitis et al. 2020). Previous studies have shown that the $\beta - 1$ parameter depends on the impact velocity and angle (S. Chourey et al. 2020; S. D. Raducan et al. 2022a), target properties (i.e., density, material strength, porosity, rotational effects; M. Bruck Syal et al. 2016; S. D. Raducan et al. 2019; R. Luther et al. 2022; A. M. Stickle et al. 2022), and surface and subsurface structures (J. Ormö et al. 2022; M. E. DeCoster et al. 2024; S. D. Raducan et al. 2020, 2024). The impactor properties for the DART spacecraft and the impact location are outlined in R. T. Daly et al. (2023). Although the calibrated images from Didymos Reconnaissance and Asteroid Camera for Optical navigation (DRACO) show that the surface and the impact site are peppered with boulders (R. T. Daly et al. 2023), subsurface features and material properties remain unclear.

The assumed complex, heterogeneous internal structure of rubble-pile asteroids is challenging to represent in numerical simulations and laboratory-scale experiments for the estimation of deflection efficiency. Surface boulders may cause an armoring effect in which the boulders behave like armor and reduce crater size (E. Tatsumi & S. Sugita 2018). The armoring effect reduces the $\beta - 1$ parameter and the cratering efficiency substantially (J. Ormö et al. 2022; M. E. DeCoster et al. 2024). On the other hand, combinations of subsurface boulders could have an anti-armoring effect and amplify the $\beta - 1$ parameter (M. E. DeCoster et al. 2024). To understand the effect of multiple boulder interactions on the ejecta momentum transfer efficiency, a full 3D model is required. The DART spacecraft impacted the local horizontal surface at $73° \pm 7°$. Most previous studies focused on vertical impact simulations. Therefore, the effect of impact angles on rubble-pile asteroids requires additional work (e.g., A. M. Stickle et al. 2015; S. D. Raducan et al. 2022a).

In this study, we take advantage of a three-dimensional shock physics code and simulate various oblique impacts. Based on previous efforts and data from the DART mission, we employ similar material and impact settings for comparison. We focus on the role of impact angle and position of large buried boulders on the vertical ejecta momentum transfer efficiency. Onboard instruments of the Hera mission will characterize both the DART impact crater and the interior of Dimorphos (P. Michel 2022). In this paper, we also present the amount of impact melt for various boulder arrangements and impact angles to investigate how much of the impact-induced melt could be deposited on the surface of Dimorphos that can be possibly seen by Hera spacecraft.

2. Methods

We use the iSALE-3D shock physics code (D. Elbeshausen et al. 2009; T. M. Davison et al. 2011) to simulate oblique impacts onto a variety of subsurface boulder arrangements. The iSALE shock physics code is a multi-material, multi-rheology extension of the SALE hydrocode (A. A. Amsden et al. 1980). Both 2D and 3D versions of the code share the same material modeling procedures, including strength models for impacts into geological targets (G. S. Collins et al. 2004) and a porosity compaction model (K. Wünnemann et al. 2006). iSALE-2D has been benchmarked against other hydrocode (R. Luther et al. 2022) and has been used for other DART-like impact studies (i.e., M. E. DeCoster et al. 2024; S. D. Raducan et al. 2019, 2022b, 2020). iSALE-3D allows for modeling oblique impacts and heterogeneous target setups. For a more detailed description, we refer to T. M. Davison et al. (2011) and D. Elbeshausen et al. (2009).

We use a similar material and impact setting to those in M. E. DeCoster et al. (2024) and S. D. Raducan et al. (2022b). Here we provide only a brief description and highlight key parameters. In previous studies, the DART impactor is often modeled as a hollow aluminum cylinder. This is justified by the fact that the impactor geometry and composition only slightly affect β (M. E. DeCoster et al. 2022; S. D. Raducan et al. 2022b). As the present version of iSALE-3D does not allow considering different materials that may mix upon impact, in our simulations we assume for the impactor a spherical basaltic (see Table 1) boulder with a radius of 0.4 m, mass (m) of 657 kg, and impact velocity (U) of 6.5 km s^{-1}, which has a similar impact kinetic energy to the DART aluminum impactor. The pre-impact surface consists of homogeneous regolith in

Table 1
Material Model Inputs for iSALE Simulation

Description	Regolith	Impactor and Boulder
Material	Basalt	Basalt
Equation of state (EOS)	Tillotson[a]	Tillotson
Poisson ratio	0.25	0.25
Strength model	LUND[b]	ROCK[c]
Thermal Parameters[d]		
Simon constant	4.5D9	4.5D9
Simon exponent	3	3
Melting temperature (K)	1360	1360
Thermal softening constant	0.7	0.7
LUND Strength Model Parameters		
Yield strength at zero pressure (Pa)	10	⋯
Maximum strength (GPa)	0.1	⋯
Internal friction coefficient	0.85	⋯
ROCK Strength Model Parameters, Intact/Damaged Surface		
Cohesion (Pa)	⋯	1D6/10
Maximum strength (GPa)	⋯	0.5/0.1
Internal friction coefficient	⋯	1/0.85
Porosity model[e]		
Porosity (%)	20	7.4
Initial distension	1.25	1.08
Elastic threshold	−1.88E−07	−1.88E−04
Transition distension	1	1
Compaction coefficient	0.9	0.9
Sound speed ratio	1	1

Notes.
[a] J. H. Tillotson (1962).
[b] N. Lundborg (1968).
[c] G. S. Collins et al. (2004).
[d] F. Simon & G. Glatzel (1929).
[e] K. Wünnemann et al. (2006).

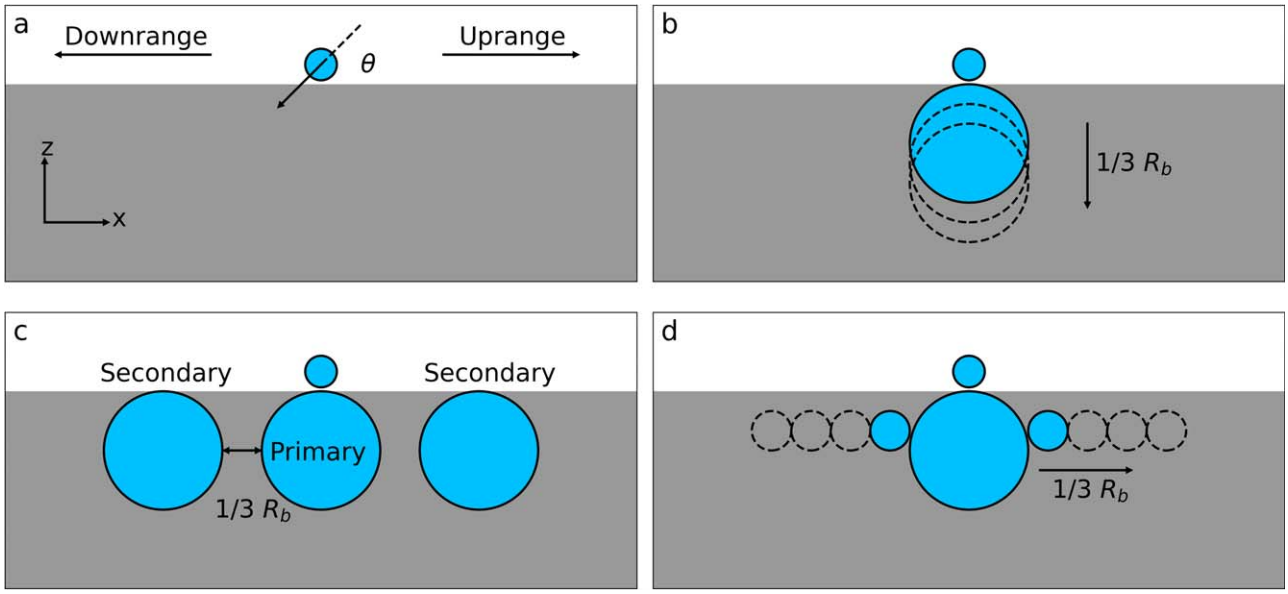

Figure 1. Model setting snapshots for different subsurface boulder arrangements. (a) Impacts on a homogeneous layer without boulders. (b) Impacts on a fully buried boulder ($R_b = 1.5$ m) with changing burial depth, $1/3\ R_b$ deeper each time. (c) Impacts on a fully buried boulder surrounded by two other boulders with the same size and separated by $1/3\ R_b$. (d) Impacts on a fully buried boulder surrounded by two other small boulders with radii of $1/3\ R_b$; each simulation increases the separation by 0.5 m. The direct-contact boulder is the primary boulder, and the rest are secondary boulders. The impact direction is from the right to the left.

which boulders different in size, depth, and arrangement are embedded (Figure 1).

In our simulations, we use the $\varepsilon-\alpha$ porosity compaction model (K. Wünnemann et al. 2006) to describe the volume behavior of both the boulder and the regolith. The porosity of boulders and regolith is 7.4% and 20%, respectively. The grain density of basalt is 2650 kg m^{-3}. Therefore, the bulk density of regolith and basaltic boulders is 2120 and 2454 kg m^{-3}, respectively. This is within the Dimorphos bulk density range suggested by A. F. Cheng et al. (2023) and S. D. Raducan et al. (2024). We use the LUND strength model (N. Lundborg 1968) for the regolith. The regolith cohesive strength is set to be 10 Pa to represent a weak layer. The boulder is significantly stronger (1–10 MPa) and denser than the surrounding regolith. We used a strength- and pressure-dependent rock strength model (G. S. Collins et al. 2004) to mimic boulder responses. Table 1 lists the full details of material model parameters.

iSALE-3D uses an *x*-*y*-*z* Cartesian coordinate system. The computational domain is a quarter-space in the positive *y*-direction (cross-range of the impact), with the *x*-*z* plane acting as a plane of symmetry, to reduce computational costs (D. Elbeshausen et al. 2009; T. M. Davison et al. 2011). We adopt a spatial resolution of 8 cells per projectile radius (CPPR) inside a high-resolution zone of $254 \times 90 \times 150$ cells for the and vertical directions, respectively. The cubic computational cells have a side length of 0.05 m. Beyond the high-resolution zone, cell dimensions incrementally increase by factors of 1.05 to reduce computational costs, and the mesh boundaries are placed far away from the cratering region to minimize adverse effects of reflection from the boundaries. The entire computational domain has a physical size of $20 \times 7 \times 13$ m. Each cell of the high-resolution zone contains a Lagrangian tracer to record material motion and physical properties. The ejecta launch velocities are recorded once a tracer leaves the transient crater and crosses the pre-impact surface (X.-Z. Luo et al. 2022). Previous studies show that the ejecta behavior in iSALE-3D and 2D simulations with the same resolution are nearly identical (X.-Z. Luo et al. 2022; S. D. Raducan et al. 2022a).

When compared to the results of high-resolution (e.g., 40 CPPR; S. D. Raducan et al. 2022a) models, low-resolution (e.g., 5 CPPR; S. D. Raducan et al. 2022a) models fail to resolve the fastest ejecta and tend to underpredict the cumulative ejecta momentum (e.g., by ∼10%; S. D. Raducan et al. 2022a). Our 3D simulations of 8 CPPR are expected to systematically underestimate the $\beta-1$ parameter by less than 10% when compared to a high-fidelity 40-CPPR model. While the full impact analysis on low-strength bodies usually requires a long simulation time, we stop our simulation at 100 ms to reduce the expensive computational cost of 3D models. Each of the 3D models utilizes over a million tracers and requires approximately 5 days to run on multiple computer cores. Our computational data indicate that 100 ms is sufficient to analyze the relative effects of boulder arrangements and impact angles on $\beta-1$. This is because, although the crater growth is not ceasing at 100 ms (see Figure A1(a)), the comparison to 2D results with a long runtime of 2 s in previous literature (M. E. DeCoster et al. 2024) shows that our 3D models produce consistent relative changes in $\beta-1$ as a function of boulder arrangements (Figure A1(b)).

The impactor momentum vector, the surface normal vector, and the ejecta momentum vector are usually not coplanar. Full three-dimensionality of momentum transfer is described in other studies (e.g., A. S. Rivkin et al. 2021; T. S. Statler et al. 2022). Generally, the orbital change of an asteroid along the surface normal component (*z*-axis in this paper) denotes the amount of effective deflection. Therefore, the vertical ejecta momentum is often the primary goal for deflection studies. The rest of the ejecta momentum will also modify the orbital change and potentially the rotation rate. In this paper, the $\beta-1$ parameter refers to the vertical momentum transfer efficiency, rather than the net momentum in all directions. M. E. DeCoster et al. (2024) showed that the transition between armoring effect and anti-armoring effect for direct

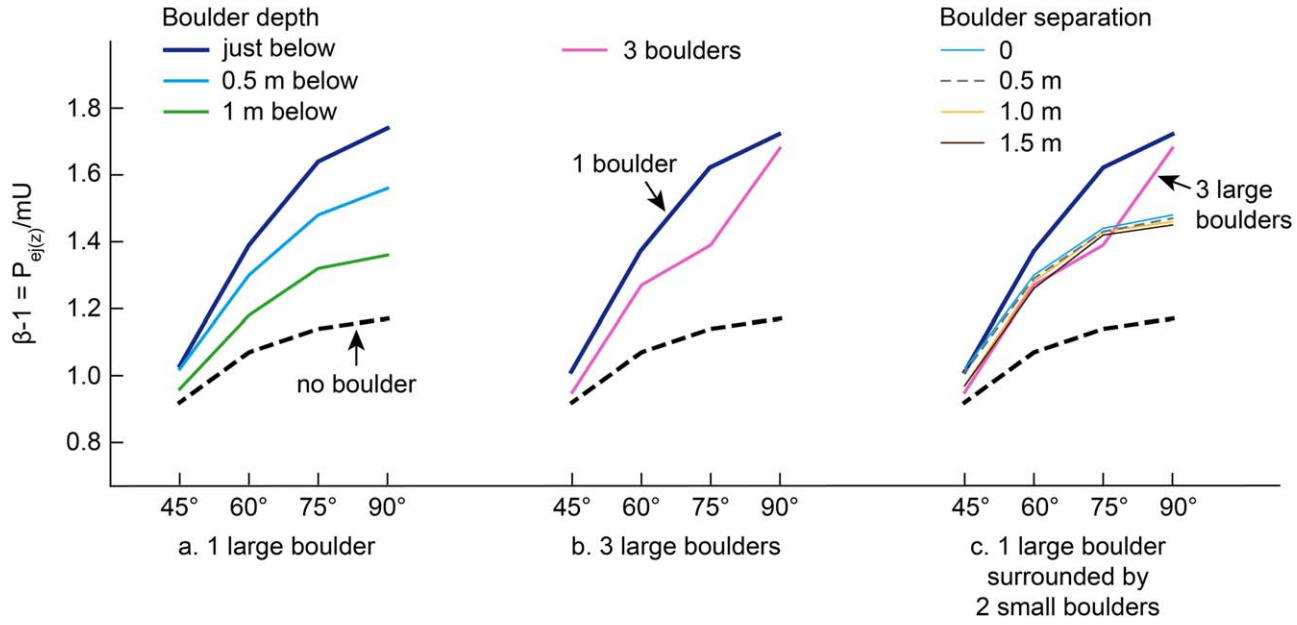

Figure 2. Vertical momentum transfer efficiency $\beta - 1$ (at 100 ms after impact) as functions of impact angle for different subsurface boulder arrangements (see Figure 1 for details). Values of $\beta - 1$ for impacts on a homogeneous regolith (dashed black line) and on a single buried boulder just below the surface (dark blue line) are plotted as reference cases in panels (a)–(c).

boulder contact depends on the size and burial depth of the boulder: surface boulders introduce an armoring effect, fully buried boulders induce anti-armoring, and boulders smaller than the impactor reduce both effects. We focused on 3D simulations of subsurface boulders since they are not directly observable. To study the response of the $\beta - 1$ factor for various impact scenarios, we chose four distinct cases: (a) impacts on a homogenous regolith (Figures 1(a)); (b) impacts on a fully buried boulder with boulder radius $R_b = 1.5$ m (3.75 times larger than the impactor), where the boulder burial depth increases by $1/3$ R_b (0.5 m) between each case (Figures 1(b)); (c) impacts on a fully buried boulder with two secondary boulders $1/3$ R_b (0.5 m) away from it and buried at the same depth (Figures 1(c)); (d) impacts on a fully buried boulder situated between two smaller boulders (with radius of 0.5 m), where the bottoms of the small boulders align with the center of the big boulder. In each case studied, the separation of the smaller boulders increased by $1/3$ R_b (see Figure 1(d)). For each case simulated, we consider four different impact angles: 45°, 60°, 75°, and 90°.

To quantify the generated impact melt, we use the classical peak pressure method (E. Pierazzo et al. 1997) while considering target porosity (K. Wünnemann et al. 2008). We estimate the melting pressure of porous basalt using the analytical equations of state (ANEOS; S. L. Thompson 1990) following T. Liu et al. (2022). The critical pressure of melting is 27 GPa for the regolith (20% porosity) and 48 GPa for the boulder (7.4% porosity). We quantify the total volume of shock-induced melt by summing up the volumes of all tracers that are shocked above the critical melting pressure. Note that the tracer's volume is given by the volume of the cell in which each tracer was initially located. We then distinguish ejected melt by tracking whether a given tracer is ejected above the pre-impact surface by the end of the simulation. We consider all non-ejected melt to be retained inside the crater.

3. Results

In this work, we carried out 36 oblique impact simulations in total. For each simulation, we integrate the product of ejecta launch velocity and ejected mass to calculate the $\beta - 1$ parameter at a time of 100 ms after impact. We then analyze the effect of impact angle and subsurface boulder arrangements on $\beta - 1$. Our simulation results are summarized in Figure 2 and Table 2. For a direct comparison of vertical ejecta momentum, we chose not to normalize our results using the impact angle-scaled vertical momentum (mUsinθ) as done in previous studies (e.g., S. D. Raducan et al. 2022a; A. M. Stickle et al. 2022). Instead, we used the impactor's total momentum (mU) for normalization.

3.1. Effects of Oblique Impacts for a Homogeneous Regolith Target

We first use iSALE-3D to perform oblique impact simulations on a homogeneous regolith layer as reference cases (Figure 1(a)). Figure 3(a) shows the resulting cumulative $\beta - 1$ as a function of normalized vertical ejection velocity (ratio of vertical ejecta velocity V_z and impact velocity U). $\beta - 1$ parameters are y-intercept points for each simulation case. From both Figures 2 and 3 we can see that impact angle has a strong effect on the $\beta - 1$ value at 100 ms after impact. The greatest $\beta - 1$ value occurs when the impact is vertical, which is about 1.17. This value gradually decreases as the impact becomes more oblique. For a 75° impact the $\beta - 1$ factor is 1.14, about the same as the vertical impact. The vertical momentum transfer efficiency drops to 0.92 for a 45° impact, reduces by 21% compared to a 90° impact. This implies that the impactor's incident momentum (mU) is greater than the total vertical momentum of ejecta. The decrease of $\beta - 1$ with impact angle is also observed in previous iSALE-3D simulations by S. D. Raducan et al. (2022a) (see Table 2).

Obliquity enhances the difference in $\beta - 1$ of uprange and downrange ejecta. The $\beta - 1$ of downrange and uprange ejecta

Table 2
Values of $\beta - 1$ for Different Impact Angles and Subsurface Boulder Arrangements from iSALE-3D and iSALE-2D Simulations

	Impact Angle, θ				
Boulder Arrangements	45°	60°	75°	90°	90° (2D)
One boulder, just below	1.03	1.39	1.64	1.74	1.85 (This study) 2.8 (M. E. DeCoster et al. 2024)
One boulder, 0.5 m below	1.02	1.30	1.48	1.56	1.71 (This study) 2.6 (M. E. DeCoster et al. 2024)
One boulder, 1 m below	0.96	1.18	1.32	1.36	1.57 (This study) 2.4 (M. E. DeCoster et al. 2024)
Three boulders, just below	0.95	1.27	1.39	1.68	1.73
One boulder and two small boulders, 0 m separation	1.02	1.30	1.44	1.48	1.81
One boulder and two small boulders, 0.5 m separation	1.01	1.29	1.43	1.47	1.82
One boulder and two small boulders, 1 m separation	0.97	1.28	1.43	1.46	1.83
One boulder and two small boulders, 1.5 m separation	0.97	1.26	1.42	1.45	1.84
No boulder	0.92	1.07	1.14	1.17	1.45 (This study) 2.3 (M. E. DeCoster et al. 2024)
No boulder (S. D. Raducan et al. 2022a)	0.94	1.18	⋯	1.32	⋯

Note. Note that the $\beta - 1$ values in S. D. Raducan et al. (2022a) are originally defined as the total vertical ejecta momentum normalized by the vertical component of the impact velocity, and values in the table have been multiplied by $\sin(\theta)$ for a consistent comparison. $\beta - 1$ is calculated at 0.1, 1, and 2 s post-impact, respectively, in this study, S. D. Raducan et al. (2022a), and M. E. DeCoster et al. (2024).

are identical for a 90° impact. The smaller the impact angle, the greater the contribution of downrange ejecta to the total ejecta momentum. For a 45° impact on a homogeneous regolith, the downrange ejecta ($\beta - 1 \approx 0.67$) are responsible for 73% of total vertical ejecta momentum.

Figure 3(b) shows the excavation zone with normalized vertical ejection velocity for different impact angles. For a more oblique impact, the downrange direction tends to produce more ejecta, causing the asymmetrical ejecta distribution (X.-Z. Luo et al. 2022). More vertical impacts on a single regolith layer produce a larger ejecta volume, which adds up to the total momentum. However, oblique impacts lead to the production of more fast-moving ejecta. This is consistent with previous DART-like impact models (A. M. Stickle et al. 2015). The fast-moving ejecta with normalized vertical velocity, $V_z/U > 0.05$ ($325\ \mathrm{m\ s^{-1}}$ before normalization), mainly originate from the impactor and within 2 m of the impact point. For oblique impacts, the fast-moving ejecta is concentrated in the downrange direction and contributes significantly to the overall $\beta - 1$ factor (Figure 3(a)), ∼40% of total $\beta - 1$ for a 45° oblique impact, while vertical impacts and 75° impacts on a homogeneous layer show a similar ejecta velocity distribution in both the uprange and downrange directions.

3.2. The Effect of Oblique Impact on Boulder Contacts

3.2.1. Single Primary Boulder

The next scenario we investigate is when the impactor strikes onto a fully buried large boulder inside the regolith, as shown in Figure 1(b). Figure 4 shows $\beta - 1$ (at 100 ms after impact) against normalized vertical ejecta velocity for a large, buried boulder ($R_b = 1.5$ m) for various impact angles and burial depths from 0 to 1 m ($2/3\ R_b$). The burial depth is the offset between the boulder top and the pre-impact surface. We also use the previous $\beta - 1$ result for a 90° impact onto a no-boulder target as our reference case. Compared to the $\beta - 1$ values for a homogeneous target, we observe an amplification of total ejected momentum for all simulations regardless of the primary boulder burial depth (Figure 2(a)). This amplification effect reaches its maximum when the primary large boulder is just below the surface (Figure 4(a)), which was identified in previous 2D simulations (see Table 2; M. E. DeCoster et al. 2024).

This amplification of total ejected momentum is called the anti-armoring effect. The high-impedance large boulder buried inside the regolith promotes impact kinetic energy transfer to its surroundings, resulting in the production of more fast-moving ejecta, as well as slow-moving ones (M. E. DeCoster et al. 2024). All simulated impacts on a single primary boulder show a substantial increase of fast-moving ejecta compared to the reference case (see Figure 4). The anti-armoring effect reaches its maximum effect when the buried object is just below the surface and disappears as the boulder is buried deeper, demonstrated by the decrease of the $\beta - 1$ parameter with the more deeply buried primary boulder (Figures 4(b) and (c)). This is because the boulder has to be within the coupling zone (i.e., zone where the impactor momentum and energy are transferred to the target) to have an effect. We will discuss that 2D models with the same runtime of 100 ms as 3D models produce a slightly higher $\beta - 1$ in Section 4.5.

We observe that the anti-armoring effect decreases with impact angle. If we take the case as an example where the boulder is initially placed just below the surface, $\beta - 1$ increases by 0.57 for the vertical impact, which is about 50% higher compared to the reference no-boulder case. For 45°, 60°, and 75° impacts, the $\beta - 1$ parameter increases by 12%, 30%, and 43%, respectively (an increment of 0.11, 0.32, and 0.5). The anti-armoring effect is weaker for oblique impacts because the boulder is offset from the trajectory of the impactor. Additionally, the momentum transfer efficiency is less sensitive to the boulder burial depth for oblique impacts than for vertical impacts. The $\beta - 1$ value for a vertical impact reduces from 1.74 to 1.36 as the boulder burial depth increases from 0 to 1 m, while the value for a 45° impact rarely changes, reducing from 1.03 to 0.96 (Figure 2(a)).

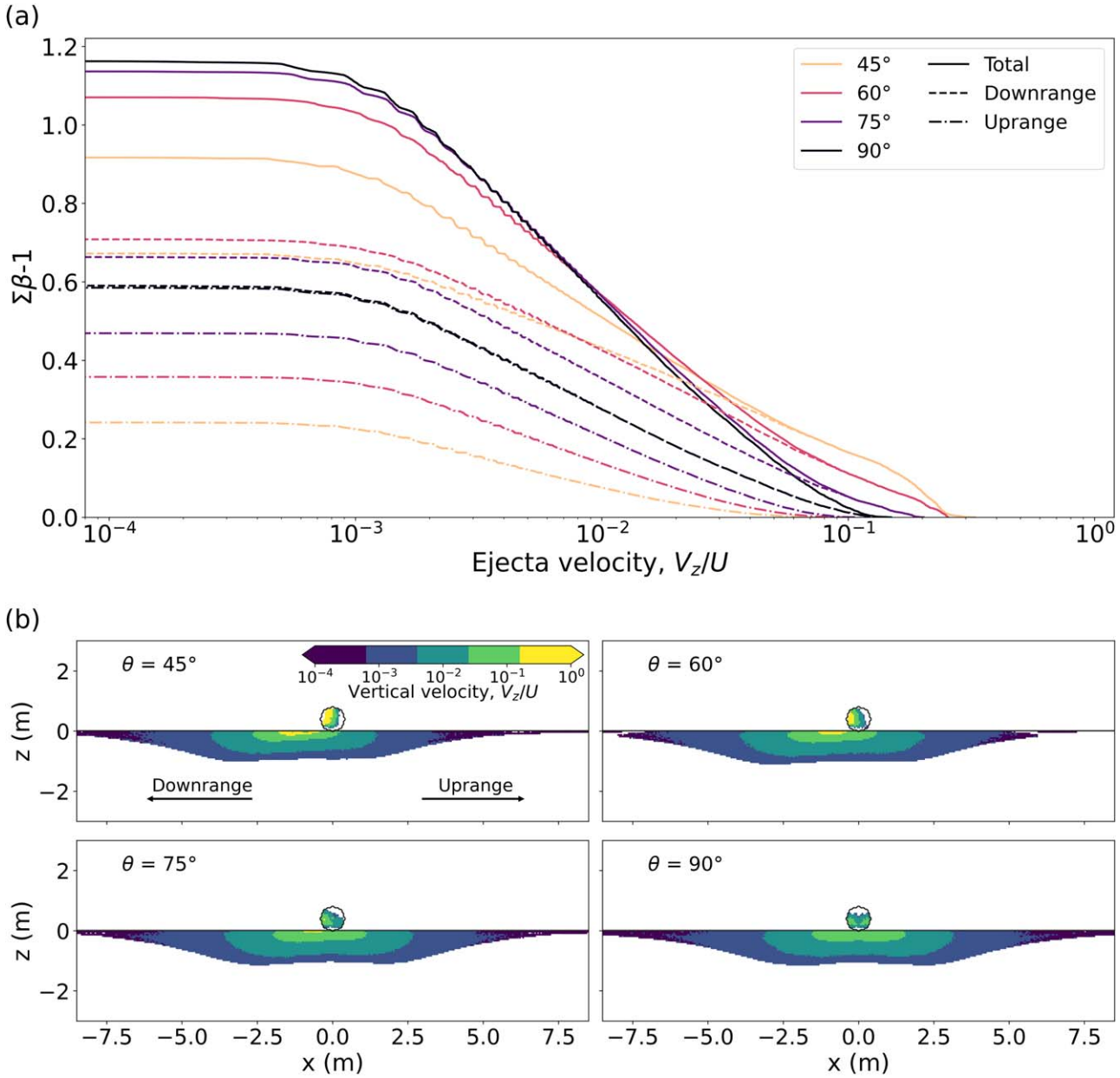

Figure 3. iSALE-3D results for (a) cumulative vertical momentum transfer efficiency $\beta - 1$ against normalized vertical ejecta velocity (V_z/U) for impacts on the homogeneous regolith with different impact angles (θ). (b) Ejecta provenance plots for various impact angles. Colors represent the normalized vertical velocity (V_z/U). Tracer ejection velocity is plotted at the pre-impact position.

3.2.2. Secondary Boulders

In the previous section, we showed that primary boulders buried under the surface have an anti-armoring effect on the momentum transfer efficiency. To examine the effect of multiple buried boulders, we placed two secondary large boulders of the same size as the primary one on either side of the primary in the trajectory direction, with separations of $1/3$ R_b (0.5 m; Figure 1(c)). Figure 5 shows the total ejected momentum at 10 ms after impact against normalized vertical velocity. The $\beta - 1$ parameter for a 90° vertical impact is 1.68. This value is considerably higher than the no-boulder case (blue line in Figure 5). Moreover, the total vertical momentum is smaller compared to the case when only a primary boulder is present inside the regolith (dashed black line in Figure 5). This indicates that the primary boulder provides a strong anti-armoring effect to the system, and secondary boulders slightly reduce it.

Figure 6 shows the peak pressure gradients and the excavation zone for impact angles of 45° and 75°. The primary boulder undergoes high shock pressure (>5 GPa; Figures 6(a) and (b)). Upon the initial impact contact on the top of the primary boulder, the amplitude of the shock wave is amplified by the boulder owing to its higher density than the surrounding regolith. Note that the secondary boulders do not significantly amplify the shock pressure (Figure 6(e)). The primary boulder material is ejected at higher vertical velocity than the secondary boulder material (Figures 6(c) and (d)). Therefore, secondary boulders do not contribute much to fast-moving ejecta and their momentum. As for the bulk mass of low-velocity ejecta, which has a main contribution to the value of $\beta - 1$, the presence of secondary boulders generally results in less ejecta. Replacing weak regolith with stronger secondary boulders dissipates more impact energy; hence, the secondary boulders have an armoring

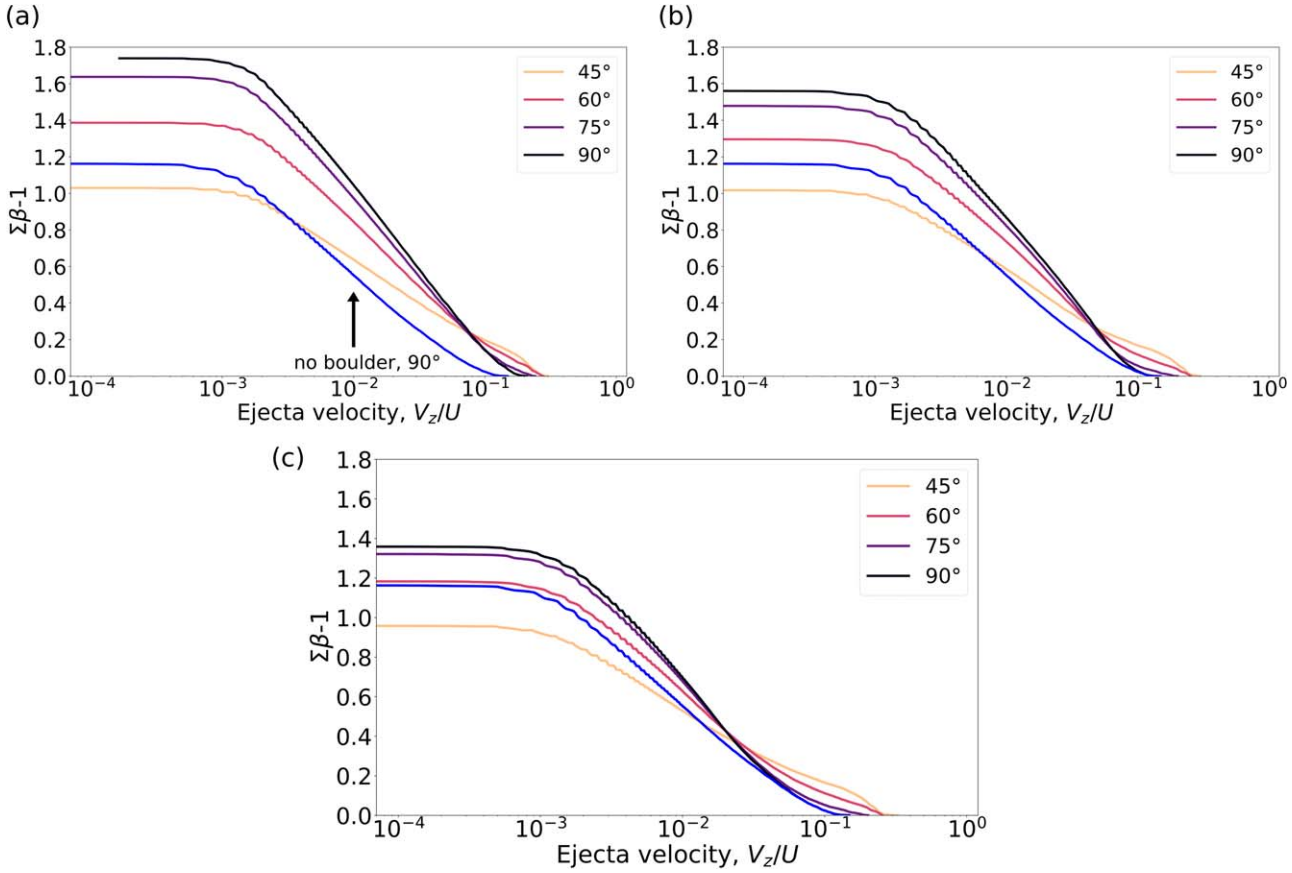

Figure 4. Cumulative vertical momentum transfer efficiency, $\beta - 1$, as a function of normalized vertical ejecta speed (V_z/U) for impact on to a single large boulder, which is buried in the regolith (a) just below the surface, (b) $1/3$ R_b (0.5 m) under the surface, and (c) $2/3$ R_b (1 m) under the surface. The solid blue line is the reference case for a vertical impact onto a homogenous layer, as shown in Figure 1(a).

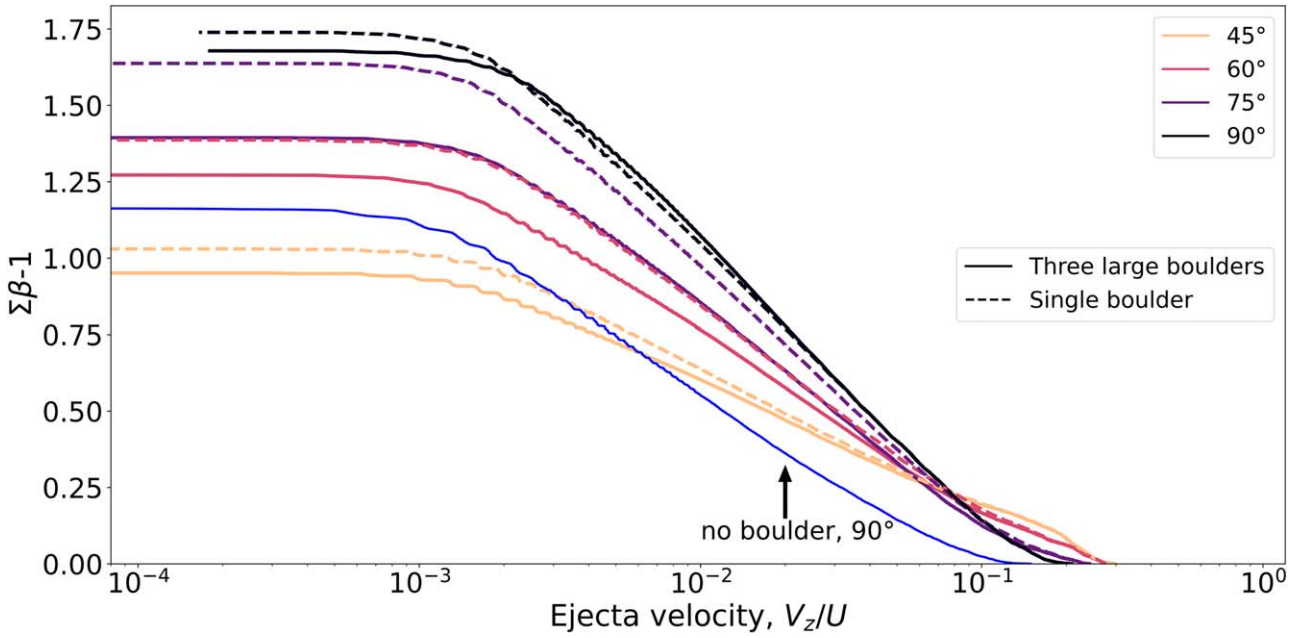

Figure 5. Cumulative vertical momentum transfer efficiency, $\beta - 1$, as a function of normalized vertical ejecta speed (V_z/U) for impact simulation setting as in Figure 1(c). Results for a single boulder (Figure 4(a)) are plotted for comparison, as shown by dashed lines. The solid blue line is the reference case for a vertical impact onto a homogenous layer, as shown in Figure 1(a).

effect on ejecta production, exhibited by relatively smaller $\beta - 1$ factors compared to the one-boulder case (see Figure 2(b)).

For a 45° oblique impact, there is significantly less uprange ejecta compared to the downrange side. The uprange secondary boulder undergoes less excavation, and there is no ejecta

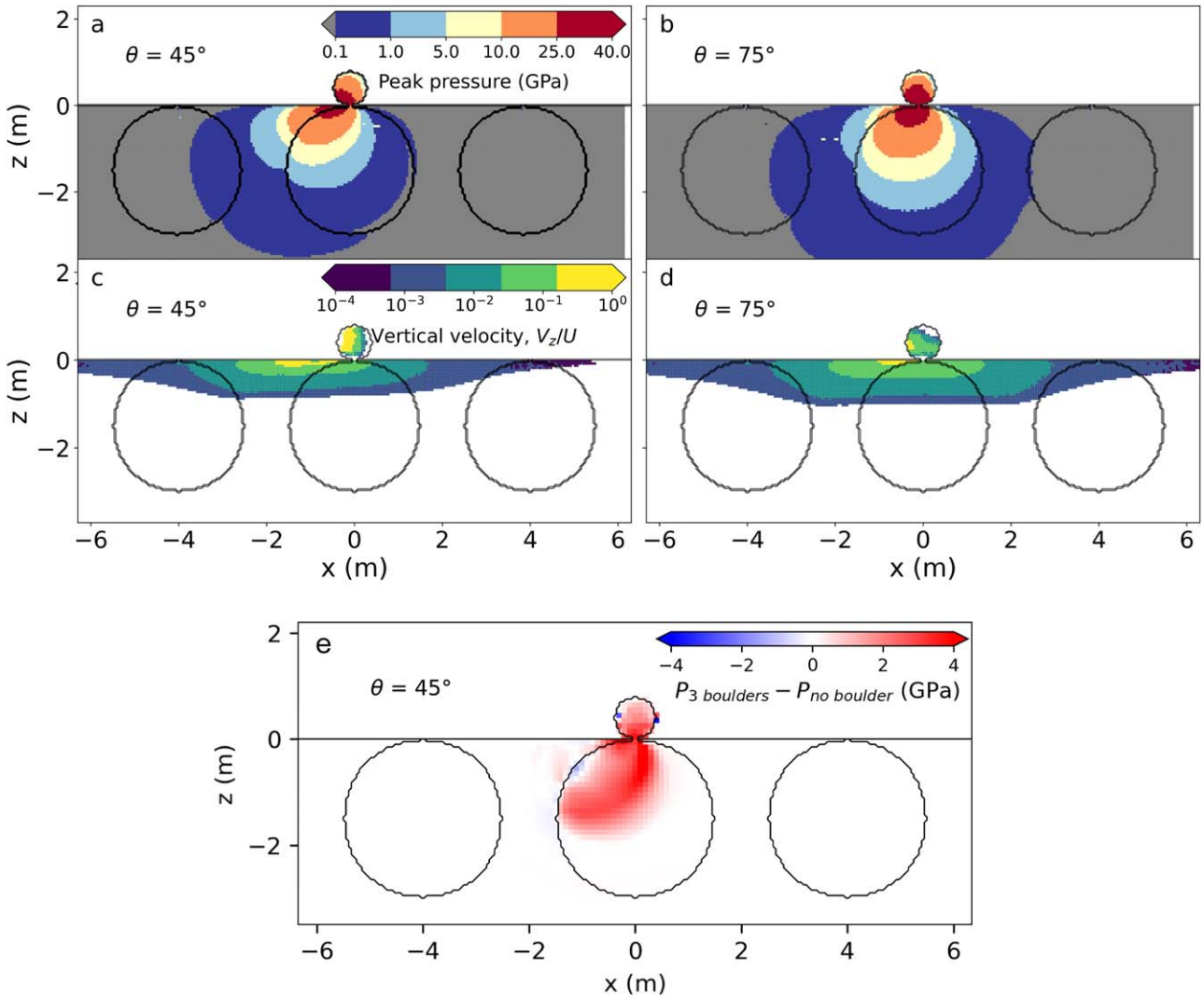

Figure 6. iSALE-3D results for (a, b) peak pressure contour plots for oblique impact angle 45° and 75° and (c, d) ejecta provenance plots for oblique impact angle 45° and 75° with normalized vertical velocity (V_z/U). Ejecta is placed at the pre-impact position. (e) Contrast of the peak pressure between targets with three boulders and targets without any boulders.

formation beyond 5.5 m. A more vertical 75° impact interacts more with the primary boulder. Both the peak pressure and ejecta distribution are approaching symmetry. Therefore, more vertical impacts are sensitive to structural changes closer to the impact point.

3.2.3. Small Secondary Boulders with Different Separation

As the subsurface structure of rubble-pile asteroids is complex, we also change the radius of the secondary boulder to 0.5 m ($1/3$ R_b) and vary their separations to the primary boulder. Figure 7 shows $\beta - 1$ values against the distance between the secondary small boulder and central primary boulder. For all impact angles, the total ejecta momentum at 100 ms after impact gradually decreases as the secondary boulders move away from the primary target. Overall, the separation between the primary and secondary boulders has little effect on the vertical momentum transfer efficiency (Figures 7, 2(c)). However, it is expected that the armoring effect would diminish if the secondary boulders were placed infinitely far away from the primary boulder, so that $\beta - 1$ is the same as for the one-boulder case.

The small secondary boulders are $1/27$ of the volume (and mass) of the larger ones. Compared to large secondary boulders, we find a generally larger $\beta - 1$ when the secondary boulders become smaller (Figures 2(c), gray dashed line and pink line). This suggests that any object buried away from the direct impact point will cause an armoring effect that is proportional to the size of the object.

3.3. Horizontal Ejecta Momentum

In this study, we express the enhancement of vertical momentum by the ejecta as $\beta - 1$. Following S. D. Raducan et al. (2022a), we express the enhancement of horizontal momentum as $\gamma - 1$. Here we define $\gamma - 1$ as the cumulative ejecta momentum in the x-direction normalized by the impactor's total momentum (mU). Materials are ejected laterally toward all directions, but oblique impacts produce asymmetric distributions of momentum in the downrange and uprange directions. The net horizontal ejecta momentum is the vector sum of the momentum in the x-direction (uprange) and negative x-direction (downrange).

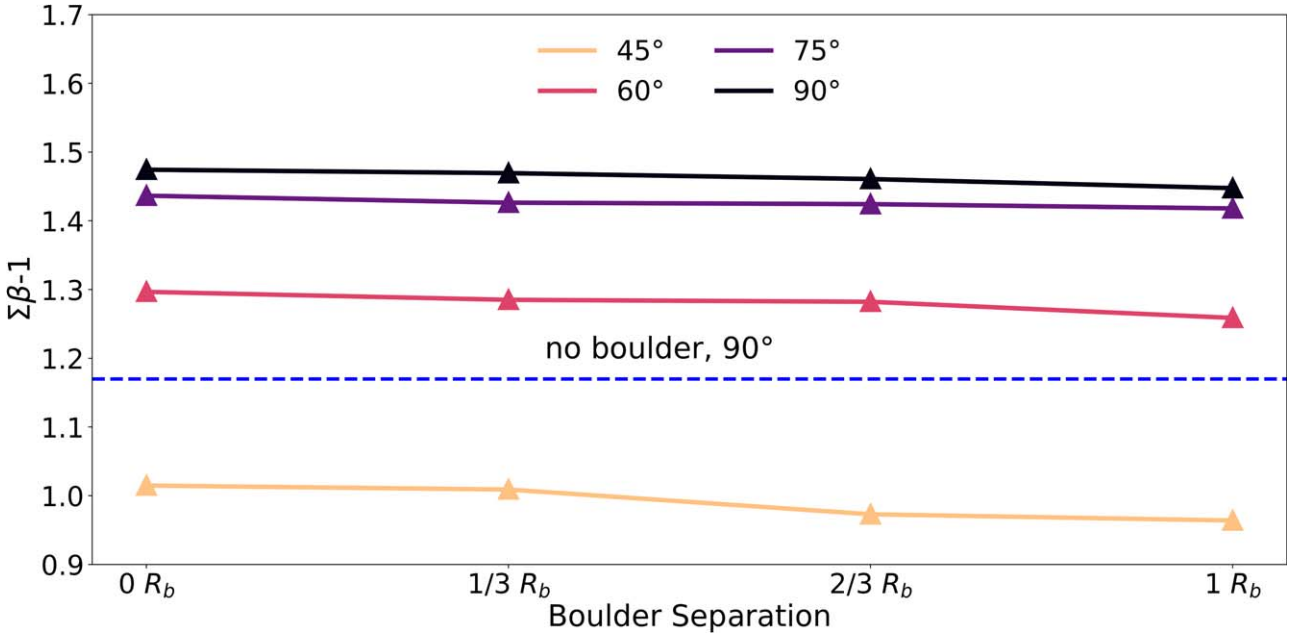

Figure 7. $\beta - 1$ as a function of separations between the primary and the secondary small boulders, where R_b is the radius of the primary boulder (1.5 m). The dashed blue line is the reference case for a vertical impact onto a homogenous layer, as shown in Figure 1(a).

In Figure 8, $\gamma - 1$ is depicted against normalized horizontal ejecta velocity for both the no-boulder simulation and the simulations with a buried boulder at different depths beneath the surface. In the case of 90° impacts, values of $\gamma - 1$ for the uprange and downrange sides sum up to 0 (Figure 8(c)), indicating that the post-impact asteroid experiences no net horizontal movement. However, for oblique impacts, there is a larger ejecta momentum toward the downrange direction (Figures 8(a) and (b)), resulting in a net ejecta horizontal momentum in the downrange, which would result in a momentum imparted to the target in the uprange (Figure 8(c)). We observe that the subsurface boulder just below the surface has an anti-armoring effect on both uprange and downrange ejecta (Figures 8(a) and (b)). The net effect is that different subsurface boulder arrangements do not significantly influence the net $\gamma - 1$ parameter (Figure 8(c)).

3.4. Impact Melt Production

The target experiences intense pressure and deformation during hypervelocity impacts. Our simulations show that the impacts at speeds of 6.5 km s^{-1} cause a shock wave with maximum pressure amplitudes of ∼40 GPa for impact angles between 45° and 90° on the monolith. For models with a boulder directly buried below the impact point, the maximum pressure amplitudes are ∼45 GPa for impact angles of 45°–90°. This is significantly larger than the assumed critical peak shock pressure for melting of ∼25 GPa in regolith but smaller than the critical pressure for melting of ∼50 GPa for the boulders. Materials close to the impact point experience the strongest shock (see Figure 6). Figure 9 illustrates the shock-induced melt at various impact angles for two different target configurations. For impacts on a homogeneous regolith (Figure 9(a)), melt forms in an oblate zone under the impact point. The impact angle influences the geometry of the melt zone owing to the asymmetric shock propagation in oblique impacts (Figures 6(a) and (b)). More oblique impacts produce larger amounts of melt in the downrange direction than in the uprange direction, consistent with previous numerical studies of melt production in oblique impacts (T. M. Davison et al. 2014; B. A. Ivanov & N. A. Artemieva 2002; E. Pierazzo & H. J. Melosh 2000; S. Wakita et al. 2019). The impact angle also influences the ejection and retention of melt. For lower impact angles, more melt is ejected in the downrange than in the uprange direction. The retained melt lines the wall and floor of the impact crater and is more likely preserved on the downrange wall for oblique impacts.

During the propagation of a shock wave, the pressure can be amplified when the shock wave enters a medium with a higher density. In addition, shock reflection at the interface between the two media increases the peak pressure the low-density medium experiences near the interface. For the target configuration with a large boulder directly under the impact point (Figure 9(b)), the shock pressure in and around the boulder is amplified compared to the no-boulder target (Figure 6(e)). Nevertheless, the less porous boulder has a larger critical pressure of melting compared to the regolith. The net result is that melting hardly occurs in the boulder even with an amplified peak pressure. Melt is only formed in the regolith adjacent to the boulder. The lowest impact angle in our simulations (45°) produces the largest amount of melt for this target configuration. This is because the highest shock pressure occurs in the downrange in oblique impacts, which exerts on the easily melted regolith rather than the boulder.

Figure 10 shows the total melt volume, ejected melt volume, and retained melt volume for our complete set of modeled boulder arrangements. The melt volume increases with impact angle for the homogenous target (Figure 10(a)). For the target with boulders placed at 0.5 and 1 m below the surface, the melt volume is the same as in the no-boulder case since the top of the boulder is lower than the maximum depth of the melt zone. For the target with a boulder directly under the impact point, the melt volume is systematically smaller and decreases with impact angle (Figure 10(a)). Secondary boulders surrounding the primary boulder do not interfere with the melt production, yielding the same melt volume as the one-boulder case. For an

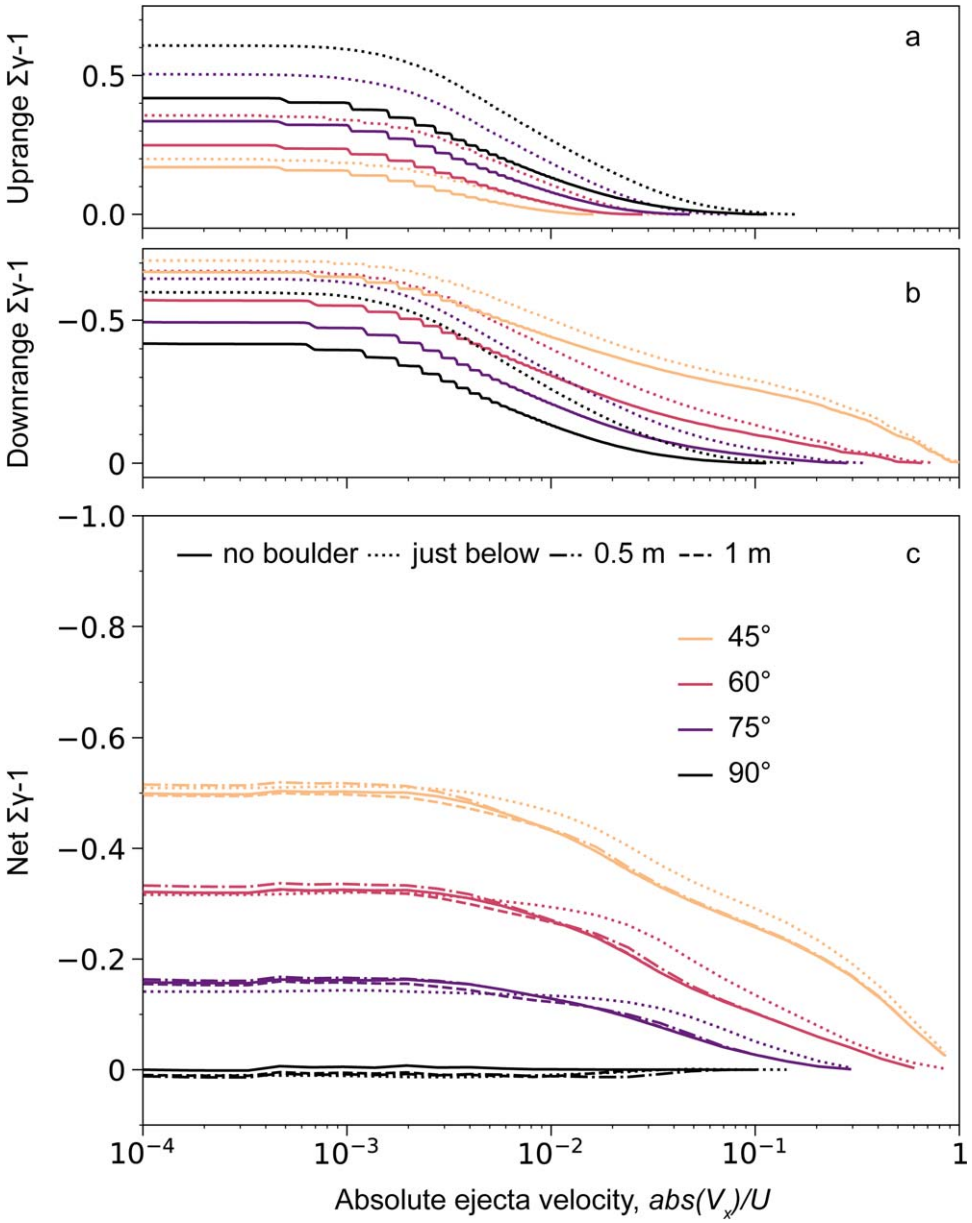

Figure 8. Horizontal momentum transfer efficiency, $\gamma - 1$, against normalized horizontal ejecta velocity (V_x/U) for (a) uprange ejecta, (b) downrange ejecta, and (c) all ejecta. Negative values of $\gamma - 1$ represent ejecta momentum toward the downrange of the impact direction. Solid lines denote impacts on a homogeneous regolith. Different styles of dashed lines denote impacts on targets with a buried boulder (see the target configuration in Figure 2(b)).

impact angle similar to the DART impact (75°), ∼0.11 m^3 of melt is produced if the impact is on a homogeneous target, and ∼0.02 m^3 of melt is produced if a boulder 3 m in diameter is buried under the impact point.

For impacts on target configurations where the melt production is not hindered by boulders (no boulder, one boulder buried below 1 m, and one boulder buried below 0.5 m), the volume of ejected melt is systematically larger for targets with buried boulders than without (Figure 10(b)). This is because boulders buried at 0.5 and 1 m below the surface do not affect melt production but have an anti-armoring effect on the ejecta, leading to the production of more ejecta and the retention of less melt (Figure 10(c)). Subsurface boulders just below the surface, although hindering melt production, have a more significant anti-armoring effect and enhance melt ejection. For 90° down to 45°, impacts on targets with a boulder directly beneath the surface (with and without secondary boulders) produce 0.015–0.020 m^3 of ejected melt, taking up 60%–75% of the total melt volume. In contrast, volumes of ejected melt for impacts on homogeneous regolith or on targets with boulders buried at 0.5 and 1 m below the surface are only 30%–50% of the total melt volumes.

The volume of retained melt is systematically larger for impacts on the homogeneous regolith than on targets with buried boulders (Figure 10(c)). Target configurations with the primary boulder directly under the impact point produce the smallest amount of retained melt. For the 75° impact (similar to the DART impact angle), 0.07 m^3 of melt is retained inside the transient crater for the homogeneous target. This value reduces to 0.054 m^3 if a boulder of 3 m in diameter is buried 0.5 m under the impact point and reduces to 0.007 m^3 if the boulder is just below the surface.

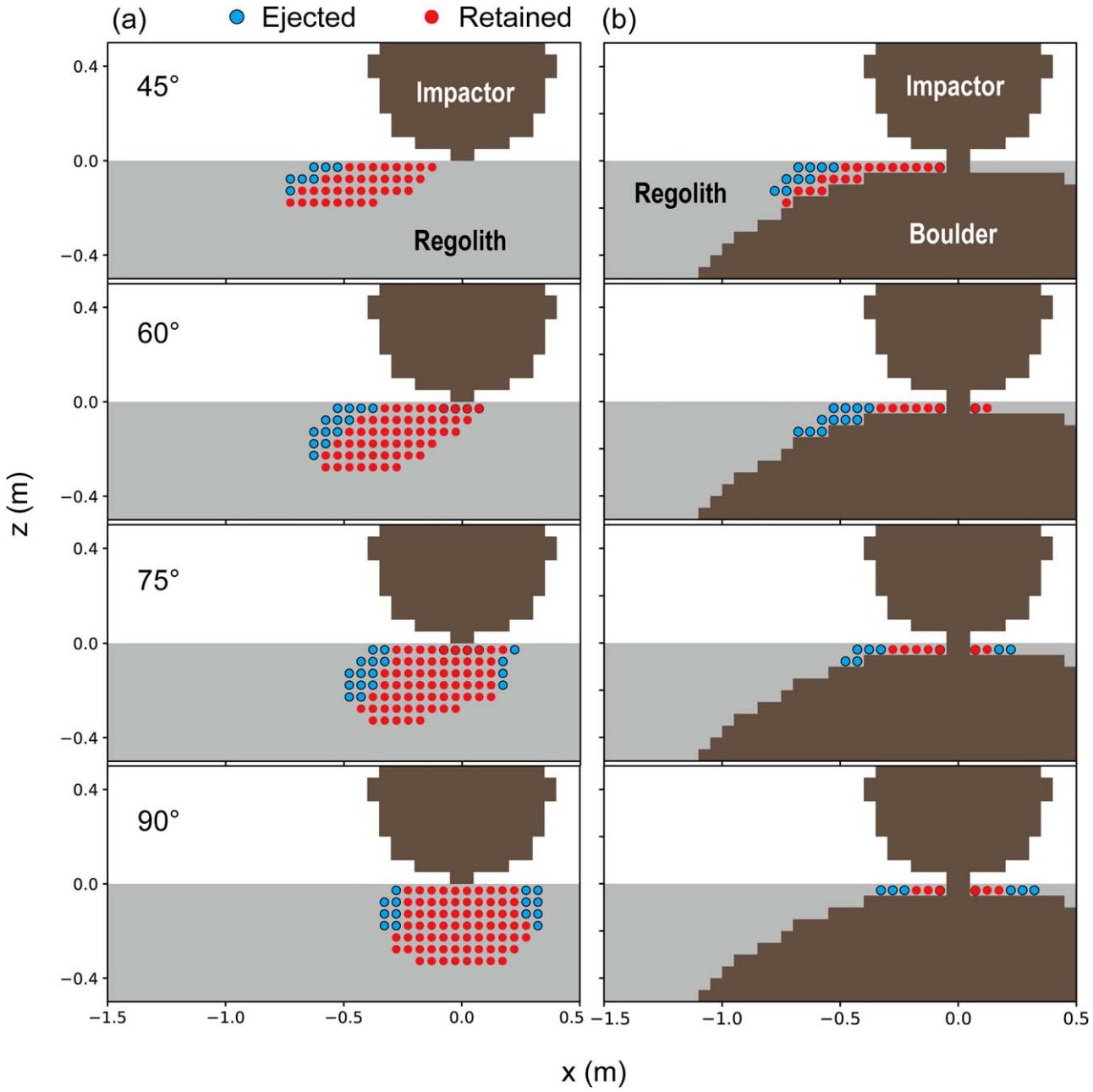

Figure 9. Shock-wave-induced impact melt for oblique and vertical (90°) impacts on (a) homogenous regolith and (b) regolith with a buried boulder ($R_b = 1.5$ m). The figures show the plane-of-symmetry cross section for 3D simulations. Circles denote pre-impact positions of melt. Blue circles denote ejected melt, and red circles denote melt retained inside the transient crater until the end of simulation at 100 ms.

4. Discussion

4.1. Effect of Subsurface Boulder Arrangements

Considering all simulations, we can estimate the effect of subsurface boulders and impact angles on the efficiency of vertical momentum transfer. Typically, more robust buried boulders can alter the $\beta - 1$ parameter by as much as 50% during a 90° impact (note that only vertical ejecta momentum has been considered). This aligns with M. E. DeCoster et al. (2024), who suggest that the global surface structure can exhibit a 3%–23% anti-armoring effect on $\beta - 1$. In this study, we focus on simple boulder arrangements near the impact point. For a real rubble-pile asteroid, boulder distributions are more complex. As shown in Sections 3.2.2 and 3.2.3, secondary boulders have an armoring effect on $\beta - 1$. The presence of more secondary boulders than simulated, which is plausible, is anticipated to reduce $\beta - 1$ even more. Our work aims at showing the relative effects of near-surface boulder configurations. With a relatively short simulation timescale (100 ms), our results remain significant as the rapid initial movement of ejecta dominates the expansion speed of the ejecta curtain (E. G. Fahnestock et al. 2022). As discussed in Section 2, the relative effects seen at 100 ms post-impact are representative of effects seen on longer timescales (e.g., Figure A1(b)).

4.2. Effect of Impact Angle

Vertical ejecta momentum decreases with obliquity. Impacts onto a homogenous layer (Figure 3) exhibit a comparable $\beta - 1$

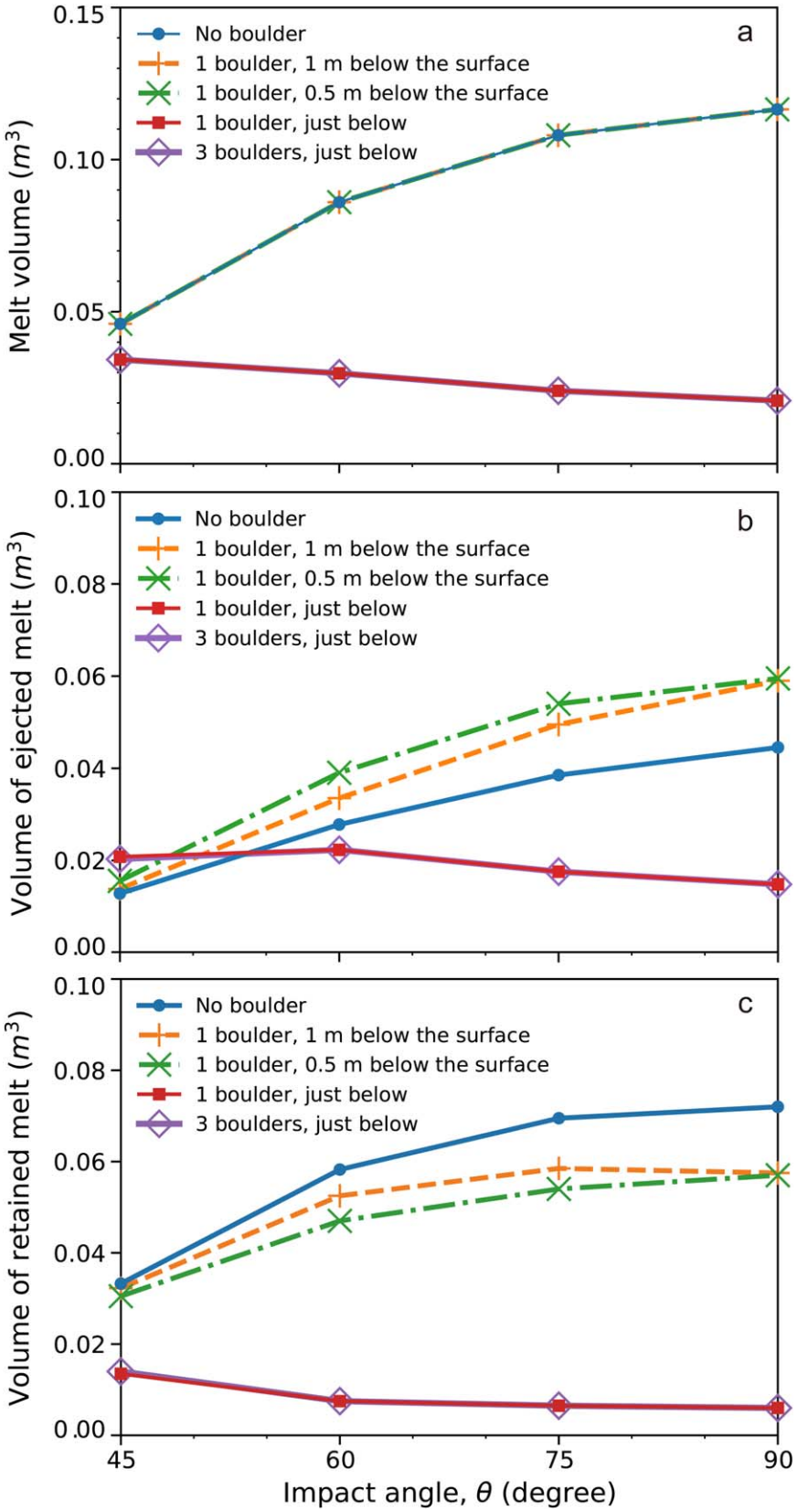

Figure 10. Volumes of (a) total impact-induced melt, (b) ejected melt, and (c) melt retained inside the transient crater for various impact angles and subsurface boulder arrangements in Figures 1(a)–(c). Retained and ejected melts are recorded until the end of simulation at 100 ms. Note that the blue, yellow, and green lines overlap, as do the red and purple lines, in panel (a).

(within a 20% range) for different impact angles. The majority of previous studies also propose that vertical ejecta momentum remains similar across various impact angles (e.g., D. Graninger et al. 2023; S. D. Raducan et al. 2022a; A. M. Stickle et al. 2022). Additionally, we demonstrated that the vertical momentum transfer efficiency ($\beta - 1$) is sensitive to impact angle when

subsurface boulders are present. The presence of a buried primary boulder induces an anti-armoring effect, increasing the overall $\beta - 1$ for all simulations. Consequently, these simulations reveal that vertical momentum transfer efficiency is sensitive to the boulder burial depth, although this sensitivity diminishes with obliquity. It appears that there is a critical angle between 60° and 75°, below which ejecta momentum experiences a dramatic drop. A. M. Stickle et al. (2022) also emphasized this observation. This offers insights into the scaling laws of oblique impacts, prompting further investigation.

In our simulations, we considered idealized scenarios where the primary boulder is directly under the impact point. In this case, the anti-armoring effect of the boulder on $\beta - 1$ is the largest for the vertical impact. However, a primary boulder offset from the impact point may change the result. We tested the case where a boulder is well within the trajectory of a 45° impact by moving the boulder to the downrange direction by 1 R_b (see Figure A2). We found that shifting the boulder reduces $\beta - 1$ by 9% for the 45° impact, indicating that the boulder directly under the impact point still has the largest anti-armoring effect on $\beta - 1$ even for oblique impacts. For a vertical impact, shifting the boulder away from the impact point laterally by the same distance reduces $\beta - 1$ by 23%.

4.3. The Role of Horizontal Ejecta Momentum

Oblique impact reduces the contribution of ejecta to vertical transfer efficiency. Oblique impacts at 45° result in a substantial amount of horizontal downrange ejecta momentum that does not contribute to vertical deflection of the orbital velocity (Figure 8). In this scenario, the vertical ejecta momentum is smaller than the impactor incident momentum ($\beta - 1 < 1$). The induced lateral momentum changes the target's trajectory along the impact direction and can cause perturbations in its rotation. A similar behavior was observed by A. M. Stickle et al. (2022) and M. Bruck Syal et al. (2016), who observed that off-axis impacts have the potential to induce perturbations in an asteroid's rotation, leading to a reduction in the linear momentum transferred during the impact. In the case of Dimorphos, such a change in rotation state modifies the mutual gravitational field between Didymos and Dimorphos, leading to an additional period change (R. Nakano et al. 2022). Future work is clearly needed on the full scale of the target to investigate the change in orbit due to oblique impacts.

4.4. Impact Melting on the Surface

Our study demonstrates that the amount of impact melt retained inside the crater may provide hints about the subsurface structure at the impact site. The simulation results show a clear distinction between the melt production on targets with and without subsurface boulders (Figures 9, 10), due to the different melting pressure of regolith and boulders. Volumes of melts retained in the crater differ by an order of magnitude for different target configurations.

To predict the appearance of retained melt, one may refer to the observed melt on other airless bodies such as the Moon. Studies of lunar impact craters show that impact melts are discernible by their low albedo and high radar circular polarization ratio (e.g., C. D. Neish et al. 2014; J. D. Stopar et al. 2014). The melts in lunar craters appear as debris-rich thin veneers or as smooth-surfaced melt ponds, depending on the volume of melt relative to the crater size. In the case of the DART impact crater, melt ponds are unlikely to form owing to the small melt volume, but small patches of melt may be observed near the impact point. Additionally, the low gravity of Dimorphos makes ejected melt unlikely to fall back on its surface. At the end of our simulations (100 ms post-impact), melts that leave the pre-impact surface are considered as ejecta. These melts, which have minimum ejection velocities of $>10\,\mathrm{m\,s^{-1}}$, will escape from the gravitation attraction of Dimorphos owing to the low escape velocity of only 0.05–0.09 $\mathrm{m\,s^{-1}}$, given the asteroid's mass of approximately (1.3–4.3) $\times$ 10^9 kg (R. T. Daly et al. 2023; K. R. Ramsley & J. W. Head 2023). Simulations that last until the end of crater formation are required to predict the melt retention better.

In our simulations, there are several limitations toward accurately predicting the distribution of melt on the surface of Dimorphos. First, resolution tests show that the melt volume increases with model CPPR (see Figure A3(a)). The low resolution of 8 CPPR in our models underestimates the melt volume by around 50%–70% compared to a high 60 CPPR (Figure A3(b)). While melting does not occur in the impactor and the subsurface boulder in the 8-CPPR model (Figure 9), it occurs in the 60 CPPR60-CPPR model (Figure A4). However, we note that melt volumes exhibit a systematic increase with CPPR for different target configurations and impact angles, and the effect of boulder presence is larger than the effect of CPPR. Second, if Dimorphos has the same bulk porosity as Didymos, which is around 30% (R. T. Daly et al. 2023), boulders and the regolith could have higher porosities than the assumed 7.4% and 20%, respectively. In this case, more melts will be produced.

We assumed a basaltic spherical impactor with a mass of 657 kg, while the DART spacecraft has a mass of 579 kg and has a more complex geometry, structure, and composition. Previous studies show that for projectile geometries with similar surface areas contacting the asteroid (e.g., sphere vs. cylinder, hollow vs. filled), the mass fractions of melting in the projectiles are similar (S. D. Raducan et al. 2022b). However, a flat-plate projectile with a much larger surface area is more prone to melting than a spherical projectile (W. Liu et al. 2024). This indicates that the solar panels of the spacecraft are more prone to melting than the central bus. Effects of spacecraft geometry on melt production in the target require further investigations with numerical simulations.

4.5. Comparison of 2D and 3D Simulations

While 3D models incur higher computational costs compared to 2D simulations, their accuracy in representing actual geometries is unparalleled. Our 3D simulations with primary and secondary boulders consider one primary spherical boulder and two secondary spherical boulders, one on either side of the primary aligned parallel to the x-direction. In a 2D cylindrical system, materials are depicted with an axially symmetric geometry. In the equivalent scenario in 2D, the secondary "boulders," which are centered around the axis of symmetry, have a toroidal shape rather than a spherical one. Compared to spherical secondary boulders, additional hoop stresses would act tangentially along the circumference of the toroid, predictably inducing different behaviors in the material motion. The mass of the boulder is also dramatically larger in the 2D/toroid case than in the 3D spherical boulder case. Consequently, the overall $\beta - 1$ behavior may vary significantly

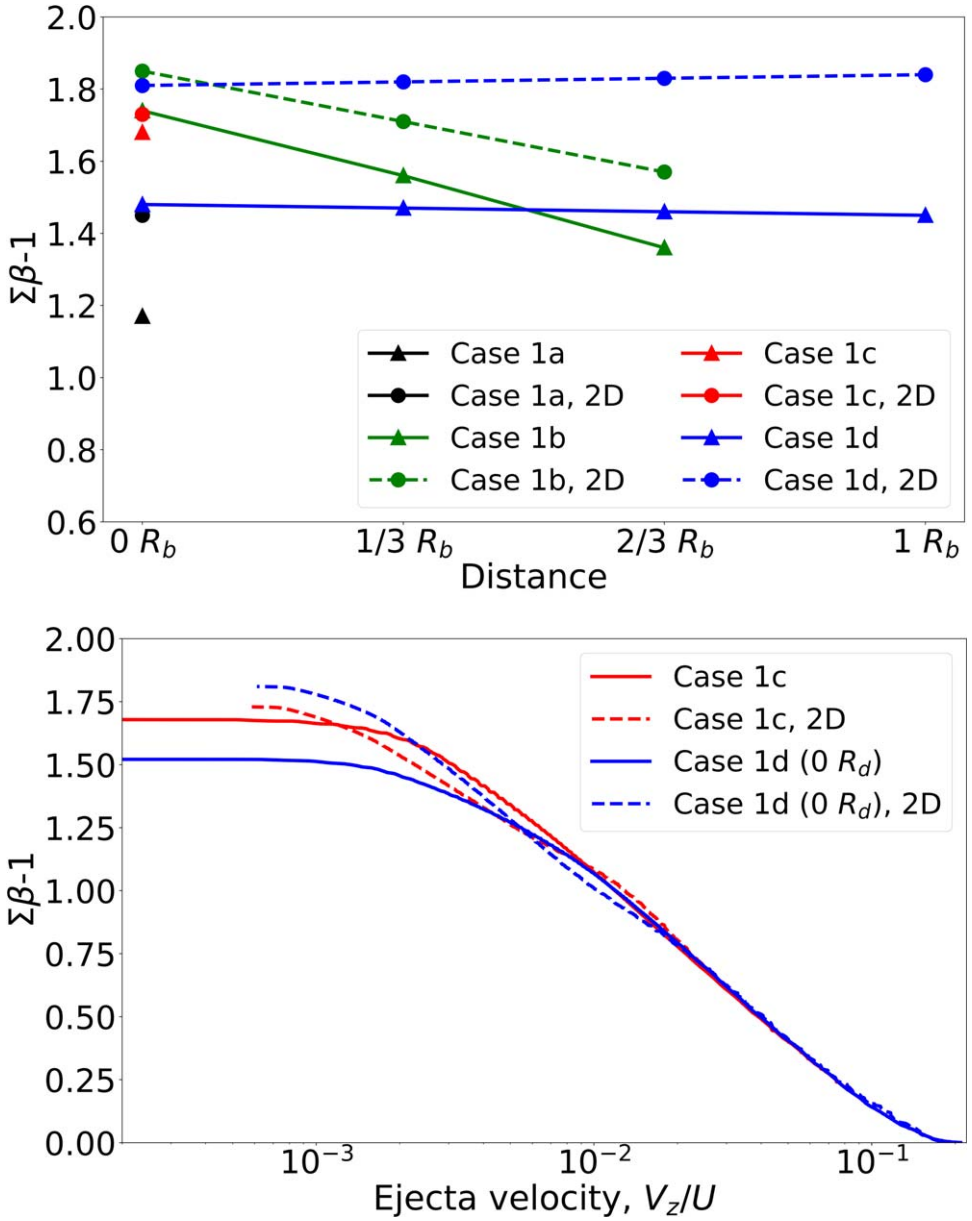

Figure 11. Comparison of total $\beta - 1$ (at 100 ms after impact) against burial depth or boulder separation for 2D and 3D vertical impact simulation as shown in Figure 1 (top) and total $\beta - 1$ against normalized ejecta velocity for 2D and 3D vertical impact as shown in Figures 1(c) and (d) (bottom). 2D simulations have the same material properties and resolution (8 CPPR) as 3D models.

between 2D and 3D representations with changing subsurface structures.

Figure 11 illustrates the $\beta - 1$ values for all vertical impact simulations, corresponding to Figure 1, alongside their respective 2D results. Whether it is the same geometry between 2D and 3D (Cases 1a and 1b) or secondary "boulders" as a toroid versus spheres (Cases 1 c and 1d), the 2D models consistently yield larger $\beta - 1$ values, with discrepancies of up to 24% in simulations without boulders. This is because 2D models with cylindrical geometry generally produce a larger ejecta volume compared to 3D models. For Cases 1 c and 1d, hoop stresses acting on the toroid are anticipated to dissipate impact energy and lead to lower ejecta velocities (M. E. DeCoster et al. 2024). Additionally, the toroid occupies more space than spheres and is expected to have a larger armoring effect (see discussion in Section 3.2.3). On the other hand, the boulder mass in the toroid case is much greater and could increase the total ejecta momentum if ejected. Our results show that the 2D model produces higher $\beta - 1$ in Cases 1 c and 1d (Figure 11). We observe comparable velocities of fast-moving ejecta and an amplification of slow-moving ejecta in 2D models (Figure 11, bottom). This unexpected result may stem from the toroid's influence, causing a greater anti-armoring effect compared to a spherical boulder in 3D, thereby magnifying the motion of slow-moving ejecta. Furthermore, this effect may elucidate why simulation Case 1d in 2D exhibits an increase in $\beta - 1$ with increasing boulder separation, while the trend is the opposite in 3D simulations. Although a fairer comparison would be to consider a ring of secondary boulders in the 3D model, this is beyond the scope of this study. In general, a 2D cylindrical system fails to provide a valid representation when handling off-axis buried boulders.

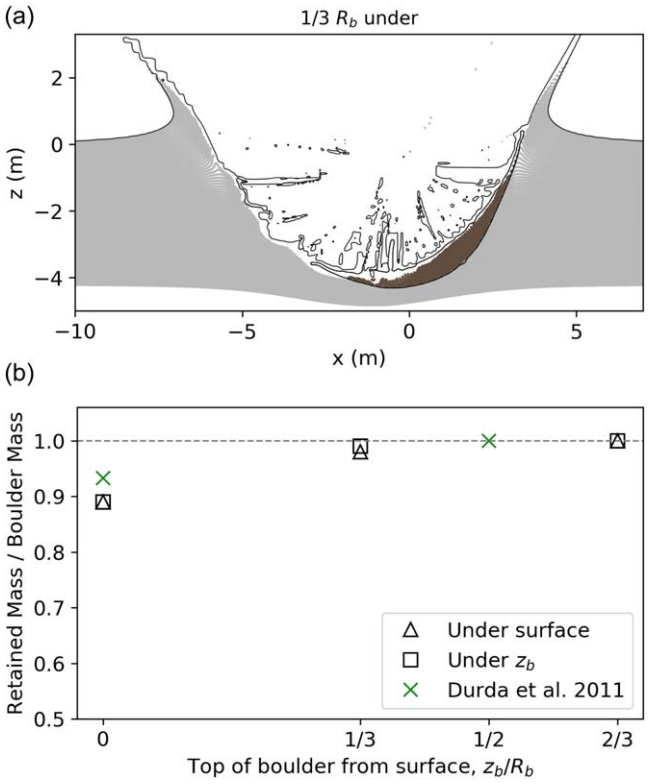

Figure 12. (a) Final step of the simulation showing locations of boulder (brown) and regolith (gray) materials for a boulder buried at $1/3$ R_b under the surface. (b) Boulder mass retained below the surface and below the burial depth as functions of the burial depth, z_b/R_b. The data points of D. D. Durda et al. (2011) are the largest remnant boulder mass divided by total boulder mass.

4.6. Validation against Impact Experiments

A critical issue in all numerical simulations is the validation of model results through comparison with experiment measurements. The ability of iSALE to model crater growth and ejecta behavior has been validated against impact experiments on water, metal, and sand (T. M. Davison et al. 2011; E. Pierazzo et al. 2008; K. Wünnemann et al. 2016). Specifically for the DART mission, R. Luther et al. (2022) validated iSALE-2D against impact experiments on regolith simulants and found that numerical models produce β values within $\pm 3\%$ of the experimental data. For regolith embedded with boulders, experiments measuring β can be challenging. Nevertheless, impact experiments have been conducted to understand boulder disruption on asteroidal surfaces (D. D. Durda et al. 2011). Here we compare our simulation results with the impact experiments by D. D. Durda et al. (2011) as an initial phase of validation. In their study, aluminum impactors are fired at 45° with a speed of 5 km s^{-1} onto granodiorite blocks that are buried at varied depths. Our target setups with one boulder (Figure 1(b)) most closely resemble their experiments, and we compare our simulated 45° impacts to their results.

We use the retained boulder mass within the crater as a function of boulder burial depth for validation. Unlike the subcatastrophic impacts conducted by D. D. Durda et al. (2011), as defined by the scaling law of K. R. Housen & K. A. Holsapple (1999), our simulations involve catastrophic impacts in terms of the impact specific energy (Q). The boulder is expected to be completely shattered, as illustrated in Figure 12(a). On the other hand, in experiments by D. D. Durda et al. (2011), the largest remnants remain within the crater, while the smaller, shattered fragments mostly leave the crater (see Figure 5 in their paper). We therefore assume that the largest remnant mass in their experiments represents the total boulder mass retained within the crater post-impact and compare this quantity to our simulations. We obtain the mass of boulder materials retained beneath the surface or the original burial depth at the end of our simulation and compare it to the results of D. D. Durda et al. (2011). The normalized retained mass as a function of boulder burial depth aligns well with the experimental data (Figure 12(b)). We expect the retained mass to decrease if our simulations run longer toward the end of crater formation. Future impact experiments in low-gravity environments or simulations that faithfully reproduce experimental conditions are required to better validate the applicability of numerical models for impacts on boulder-strewn targets.

4.7. Model Limitations

In reality, the DART spacecraft features a complex shape with various components, open spaces, and two thin solar panels. However, for this study we modeled the impactor as a basaltic sphere with similar bulk mass and impact momentum. This choice is driven by the limitations of the current version of iSALE-3D, where modeling three or more materials mixing is a challenge. Setting the impactor to be the same material as the boulder prevents such an issue. While $\beta - 1$ is only minimally affected by projectile shape (S. D. Raducan et al. 2022b), the results can vary depending on the specific geometry. J. M. Owen et al. (2022) modeled the momentum enhancement factor for different projectile geometries, including a single spherical object, multiple spheres representing the solar panels, and a more complex DART spacecraft model. They found that an idealized spherical impactor overestimates the momentum enhancement factor by 5%–15% on a strong target with approximately 100 MPa cohesion and by 10%–20% on a weak target with about 0.1 MPa cohesion. Simplifying the impactor shape also affects the distribution and formation of fast ejecta, which are produced near the impact point and influenced by the impactor's geometry.

While common numerical simulation times extend to seconds, we limited our models to 100 ms owing to the high computational cost of 3D models. Each model requires approximately 5 days to run on multiple cores, with this duration varying based on the type of computer cores used. Doubling the running time would proportionally increase the calculation time, and doubling the resolution (CPPR) would increase the running time eightfold. Although 100 ms is sufficient to reveal the relative effects of boulder arrangement and impact angle on $\beta - 1$ (Figure A1(b)), it underestimates the $\beta - 1$ value owing to the absence of late, low-velocity ejecta. Our calculated $\beta - 1$ values are systematically smaller than previous studies with the same target setups but longer runtimes (see Table 2; M. E. DeCoster et al. 2024; S. D. Raducan et al. 2022a). Additionally, a model resolution of 8 CPPR underestimates the melt volume, as discussed in Section 4.4. Convergence tests for the melt volume (Figure A3) are possible because melting occurs within a small region and a short period of time (<1 ms), so even the 60-CPPR model runs in a day. Resolution tests by S. D. Raducan et al. (2022b) using iSALE-2D show that a higher CPPR produces larger β and larger crater volume. Increasing of β and crater size with model resolution is expected in iSALE-3D simulations as well. Achieving a more

accurate measure of ejecta momentum would necessitate longer running times and higher-resolution models.

5. Conclusions

We investigate the effect of subsurface boulders and impact angles on the efficiency of vertical momentum transfer during hypervelocity impacts on rubble-pile asteroids, focusing on the case study of the DART mission targeting the Dimorphos asteroid. The study employs the iSALE-3D shock physics code to simulate various oblique impacts with different subsurface boulder arrangements. Our result shows that the vertical ejecta momentum transfer efficiency ($\beta - 1$) at early times in the cratering process is highly dependent on impact angle and subsurface structure. Compared to a monolithic surface, buried boulders near the surface amplify the deflection potential, and this effect diminishes with boulder burial depth. The direct-contact boulder dictates the deflection outcomes, with surrounding boulders hindering deflection efforts, regardless of size and separation. The deflection efficiency also decreases with obliquity. While 45° impacts significantly reduce the deflection efficiency, impacts at 75° show a similar effect to vertical impacts. Therefore, targeting buried boulders and keeping the impact angle near vertical would help to optimize deflection efficiency in DART-like impacts.

Additionally, the investigation delves into impact-induced melting on the surface, revealing that impact melt production is highly dependent on target structure at the contact point. By assuming porosities of 20% and 7.4% for the regolith and boulders, respectively, we found that for the investigated impact angles between 45° and 90° the largest volume of melt retained in the crater occurs for the 90° impact on a no-boulder regolith. Boulders buried at a depth of 0.5 m (approximately one impactor radius) under the impact point are below the maximum depth of melting caused by 6.5 $\mathrm{km\,s^{-1}}$ impacts. These boulders do not affect melt production but have an anti-armoring effect on the ejecta and increase the volume of ejected melt by 22%–40%, for impact angles of 45°–90°, compared to the no-boulder case. A boulder directly below the impact point hinders melt production and enhances melt ejection: the volume of retained melt is only 8%–40% (for impact angle from 90° to 45°) of that on a no-boulder regolith. Our results suggest that the scheduled Hera mission may observe some impact melt in the crater, and the amount of melt may provide insights into the subsurface structure at the impact site. Further studies with more realistic DART spacecraft geometry are needed to better predict the melt distribution.

Finally, our study highlights that 2D cylindrical systems fail to replicate the simulation trends observed in 3D when altering buried boulder arrangements. This suggests the necessity for future investigations to delve deeper into the disparities between 2D and 3D models, potentially expanding the scale to encompass entire asteroids.

Acknowledgments

We gratefully acknowledge the developers of iSALE (https://github.com/isale-code), in particular to Dirk Elbeshausen for developing the iSALE-3D. M.-H.Z. was supported by the Science and Technology Development Fund of Macau (0064/2022/A2; 0020/2021/A1). G.S.C and T.M.D. were supported by UK Science and Technology Facilities Council grant (ST/S000615/1).

Appendix

We stop our simulations at 100 ms post-impact to reduce the computational cost of 3D models. At 100 ms, the crater has not ceased growing (Figure A1(a)). However, compared to models that end at a later post-impact moment, our results show consistent relative changes with the boulder burial depth (Figure A1(b)). This indicates that our results remain valid concerning the relative effects of boulder arrangements on $\beta - 1$ despite the short runtime.

Simulations with a large boulder buried directly under the impact point show that the boulder has an anti-armoring effect on $\beta - 1$, and the value of $\beta - 1$ is the largest for the head-on impact and decreases as the impact turns more oblique. To test the case where a boulder is well within the trajectory of an oblique impact, we run simulations with impact angles of 45° and 90° and move the boulder horizontally to the downrange direction by 1 R_b (Figure A2(a)). The result shows that the value of $\beta - 1$ is still larger for the 90°-impact than the 45°-impact (Figure A2(b)).

In shock physics codes like iSALE, the recorded peak shock pressure is sensitive to the grid size because the shock front is concentrated in a narrow zone. The calculated volume of shock-melting thus depends on the grid resolution. In our simulations, we use a spatial resolution of 8 CPPR. Resolution tests show that the 8-CPPR models underestimate the melt volume by around 50%–70% compared to high-resolution 60-CPPR models (Figure A3). Figure A4 shows melt regions for the case with no boulder and with a direct-contact boulder. However, melt volumes exhibit a systematic increase with CPPR for different target configurations and impact angles, and the effect of boulder presence is larger than that of CPPR.

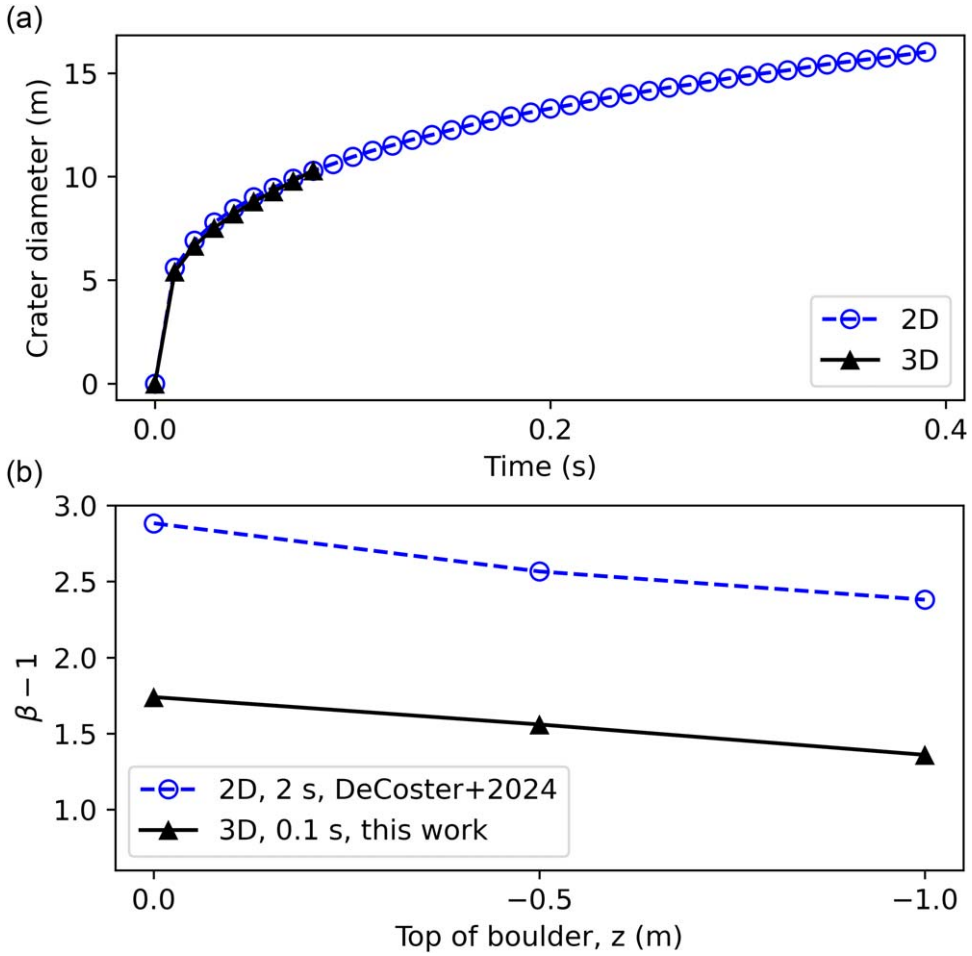

Figure A1. Comparison of crater diameter and the $\beta - 1$ parameter in 2D and 3D iSALE simulations (vertical impacts) ending at different post-impact moments. The target configuration is a single boulder buried beneath the surface (Figure 1(b)). (a) Growth of the crater diameter during the excavation stage, where the boulder is just beneath the surface. The 3D model ends at 0.1 s after impact. (b) Comparison of the $\beta - 1$ parameter in this work to the 2D results from previous literature (M. E. DeCoster et al. 2024). In their work, $\beta - 1$ is calculated at 2 s post-impact.

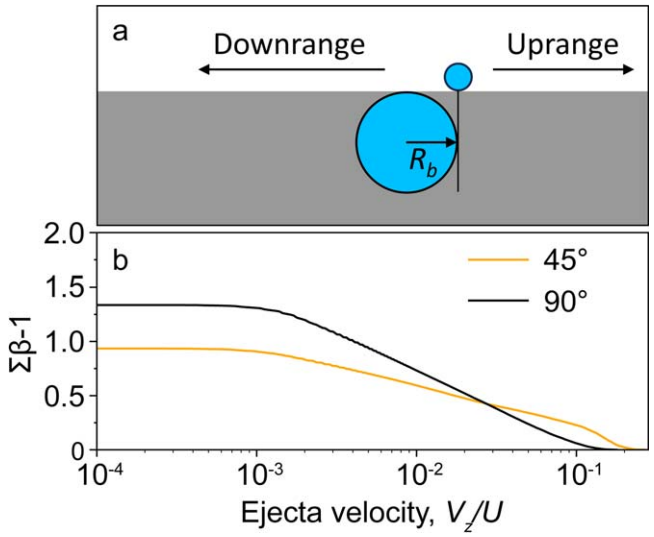

Figure A2. Test cases for a fully buried boulder placed in the downrange direction of the impact point. (a) Model setting snapshot. (b) Cumulative vertical momentum transfer efficiency $\beta - 1$ against normalized vertical ejecta velocity for impact angles of 45° and 90°. $R_b = 1.5$ m.

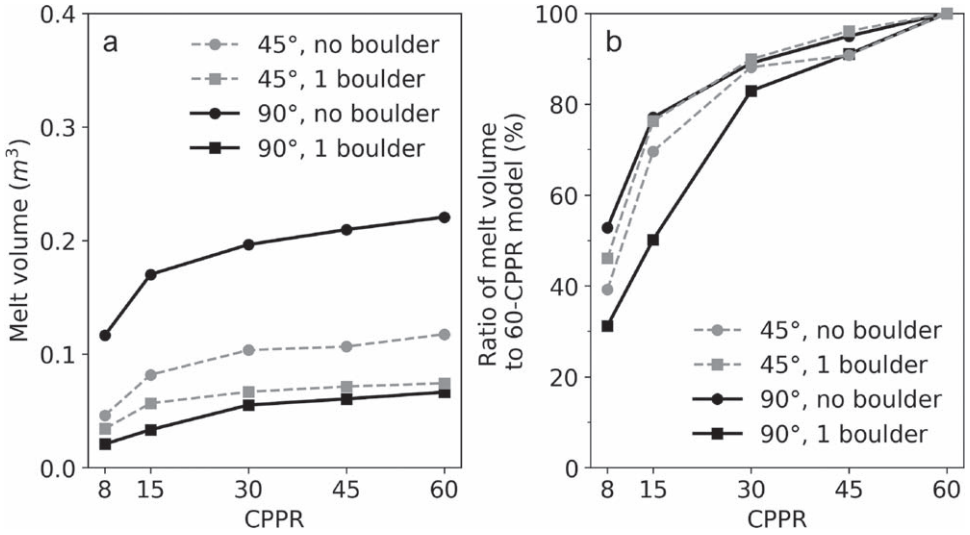

Figure A3. Resolution test for the melt volume in our simulations. (a) Volumes of total melt production and (b) volumes normalized by that of the 60-CPPR (cell per projectile radius) case as functions of CPPR. Dashed gray lines: 45° impacts. Solid black lines: 90° impacts. No boulder (circles): impacts on a monolith. One boulder (squares): impacts on a boulder buried directly below the surface ($R_b = 1.5$ m).

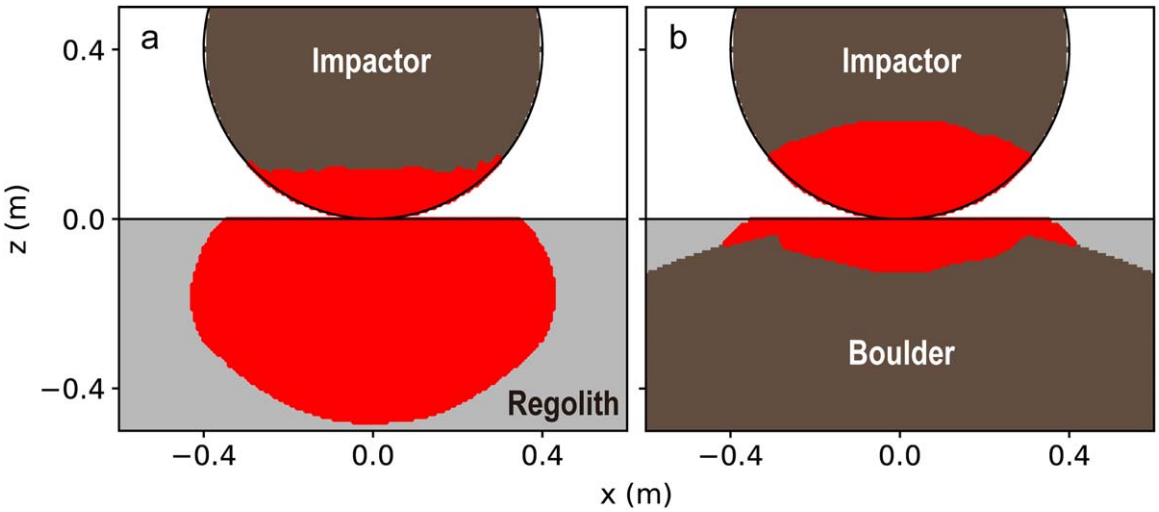

Figure A4. High-resolution (60 CPPR) modeling results of the melt region for a vertical impact on (a) homogeneous regolith and (b) regolith with a buried boulder ($R_b = 1.5$ m). Red denotes the melt region. Gray denotes the regolith, and brown denotes the impactor and boulder.

ORCID iDs

Xi-Zi Luo https://orcid.org/0000-0003-2168-7932
Meng-Hua Zhu https://orcid.org/0000-0002-8758-8243
Thomas Davison https://orcid.org/0000-0001-8790-873X

References

Abe, S., Mukai, T., Hirata, N., et al. 2006, Sci, 312, 1344
Amsden, A. A., Ruppel, H. M., & Hirt, C. W. 1980, SALE: A Simplified ALE Computer Program for Fluid Flow at All Speeds LA-8095, Los Alamos National Laboratory
Barnouin, O., Ballouz, R. L., Marchi, S., et al. 2024, NatCo, 15, 6202
Bruck Syal, M., Michael Owen, J., & Miller, P. L. 2016, Icar, 269, 50
Chapman, C. R., & Morrison, D. 1994, Natur, 367, 33
Cheng, A. F., Agrusa, H. F., Barbee, B. W., et al. 2023, Natur, 616, 457
Cheng, A. F., Michel, P., Jutzi, M., et al. 2016, P&SS, 121, 27
Chourey, S., Koschny, D., Rott, M., & Schmausser, C. 2020, P&SS, 194, 105112
Collins, G. S., Melosh, H. J., & Ivanov, B. A. 2004, M&PS, 39, 217
Daly, R. T., Ernst, C. M., Barnouin, O. S., et al. 2023, Natur, 616, 443
Davison, T. M., Ciesla, F. J., Collins, G. S., & Elbeshausen, D. 2014, M&PS, 49, 2252
Davison, T. M., Collins, G. S., Elbeshausen, D., Wünnemann, K., & Kearsley, A. 2011, M&PS, 46, 1510
DeCoster, M. E., Rainey, E. S. G., Rosch, T. W., & Stickle, A. M. 2022, PSJ, 3, 186
DeCoster, M. E., Luther, R., Collins, G. S., et al. 2024, PSJ, 5, 21
Dotto, E., & Zinzi, A. 2023, NatCo, 14, 3055
Durda, D. D., Chapman, C. R., Cintala, M. J., et al. 2011, M&PS, 46, 149
Elbeshausen, D., Wunnemann, K., & Collins, G. S. 2009, Icar, 204, 716
Fahnestock, E. G., Cheng, A. F., Ivanovski, S., et al. 2022, PSJ, 3, 206
Graninger, D., Stickle, A., Owen, J. M., & Syal, M. 2023, IJIE, 180, 104670
Housen, K. R., & Holsapple, K. A. 1999, Icar, 142, 21
Ivanov, B. A., & Artemieva, N. A. 2002, in Catastrophic Events and Mass Extinctions: Impacts and Beyond, ed. C. Koeberl & K. G. MacLeod (McLean, VA: GeoScienceWorld), 619
Liu, T., Luther, R., Manske, L., & Wünnemann, K. 2022, JGRE, 127, e07264
Liu, W., Zhang, Q., Long, R., et al. 2024, Def. Technol., 32, 89
Lundborg, N. 1968, IJRMA, 5, 427
Luo, X.-Z., Zhu, M.-H., & Ding, M. 2022, JGRE, 127, e2022JE007333
Luther, R., Raducan, S. D., Burger, C., et al. 2022, PSJ, 3, 227
Michel, P., Küppers, M., Bagatin, A. C., et al. 2022, PSJ, 3, 160
Nakano, R., Hirabayashi, M., Agrusa, H. F., et al. 2022, PSJ, 3, 148
Neish, C. D., Madden, J., Carter, L. M., et al. 2014, Icar, 239, 105
Ormö, J., Raducan, S. D., Jutzi, M., et al. 2022, E&PSL, 594, 117713
Owen, J. M., DeCoster, M. E., Graninger, D. M., et al. 2022, PSJ, 3, 218

Pajola, M., Tusberti, F., Lucchetti, A., et al. 2024, NatCo, 15, 6205
Pierazzo, E., Artemieva, N., Asphaug, E., et al. 2008, M&PS, 43, 1917
Pierazzo, E., & Melosh, H. J. 2000, Icar, 145, 252
Pierazzo, E., Vickery, A. M., & Melosh, H. J. 1997, Icar, 127, 408
Raducan, S. D., Davison, T. M., & Collins, G. S. 2020, P&SS, 180, 104756
Raducan, S. D., Davison, T. M., & Collins, G. S. 2022a, Icar, 374, 114793
Raducan, S. D., Davison, T. M., Luther, R., & Collins, G. S. 2019, Icar, 329, 282
Raducan, S. D., Jutzi, M., Cheng, A. F., et al. 2024, NatAs, 8, 445
Raducan, S. D., Jutzi, M., Davison, T. M., et al. 2022b, IJIE, 162, 104147
Ramsley, K. R., & Head, J. W. 2023, LPSC, 54, 1079
Rivkin, A. S., Chabot, N. L., Stickle, A. M., et al. 2021, PSJ, 2, 173
Robin, C. Q., Duchene, A., Murdoch, N., et al. 2024, NatCo, 15, 6203
Rozitis, B., Ryan, A. J., Emery, J. P., et al. 2020, SciA, 6, eabc3699
Simon, F., & Glatzel, G. 1929, Zeitschrift für anorganische und allgemeine Chemie, 178, 309
Statler, T. S., Raducan, S. D., Barnouin, O. S., et al. 2022, PSJ, 3, 244
Stickle, A. M., Atchison, J. A., Barnouin, O. S., et al. 2015, Procedia Eng., 103, 577
Stickle, A. M., DeCoster, M. E., Burger, C., et al. 2022, PSJ, 3, 248
Stopar, J. D., Hawke, B. R., Robinson, M. S., et al. 2014, Icar, 243, 337
Tatsumi, E., & Sugita, S. 2018, Icar, 300, 227
Thomas, C. A., Naidu, S. P., Scheirich, P., et al. 2023, Natur, 616, 448
Thompson, S. L. 1990, ANEOS Analytic Equations of State for Shock Physics Codes Input Manual SAND89-2951, Sandia National Laboratories
Tillotson, J. H. 1962, Metallic Equations of State For Hypervelocity Impact General Atomic Report GA-3216, General Atomic, San Diego, CA
Wakita, S., Genda, H., Kurosawa, K., & Davison, T. M. 2019, GeoRL, 46, 13678
Wünnemann, K., Collins, G. S., & Melosh, H. J. 2006, Icar, 180, 514
Wünnemann, K., Collins, G. S., & Osinski, G. R. 2008, E&PSL, 269, 530
Wünnemann, K., Zhu, M.-H., & Stöffler, D. 2016, M&PS, 51, 1762